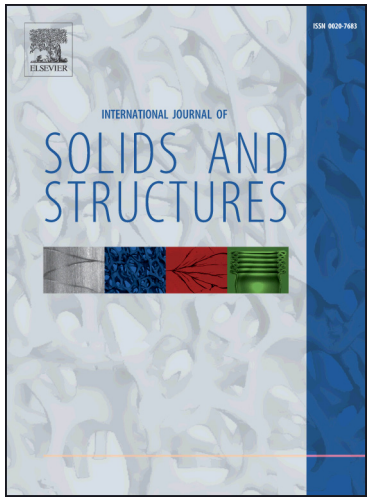

A disk-shaped domain integral method for the computation of stress intensity factors using tetrahedral meshes

Morteza Nejati, Adriana Paluszny, Robert W. Zimmerman

PII: S0020-7683(15)00244-9
DOI: http://dx.doi.org/10.1016/j.ijsolstr.2015.05.026
Reference: SAS 8791

To appear in: *International Journal of Solids and Structures*

Received Date: 31 January 2015
Revised Date: 21 May 2015

Please cite this article as: Nejati, M., Paluszny, A., Zimmerman, R.W., A disk-shaped domain integral method for the computation of stress intensity factors using tetrahedral meshes, *International Journal of Solids and Structures* (2015), doi: http://dx.doi.org/10.1016/j.ijsolstr.2015.05.026

A disk-shaped domain integral method for the computation of stress intensity factors using tetrahedral meshes

Morteza Nejati, Adriana Paluszny, Robert W. Zimmerman

Department of Earth Science and Engineering, Imperial College, London, United Kingdom
Tel: +44 20 7594 7435, Fax: +44 20 7594 7444

Abstract

A novel domain integral approach is introduced for the accurate computation of pointwise J-integral and stress intensity factors (SIFs) of 3D planar cracks using tetrahedral elements. This method is efficient and easy to implement, and does not require a structured mesh around the crack front. The method relies on the construction of virtual disk-shaped integral domains at points along the crack front, and the computation of domain integrals using a series of virtual triangular elements. The accuracy of the numerical results computed for through-the-thickness, penny-shaped, and elliptical crack configurations has been validated by using the available analytical formulations. The average error of computed SIFs remains below 1% for fine meshes, and $2-3$% for coarse ones. The results of an extensive parametric study suggest that there exists an optimum mesh-dependent domain radius at which the computed SIFs are the most accurate. Furthermore, the results provide evidence that tetrahedral elements are efficient, reliable and robust instruments for accurate linear elastic fracture mechanics calculations.

Keywords: stress intensity factor, finite element, tetrahedral, interaction integral, J-integral, unstructured mesh, 3D crack

Email address: m.nejati11@imperial.ac.uk (Morteza Nejati)

1. Introduction

Analyzing the mechanical effects of cracks in bodies has attracted great attention in a variety of scientific and engineering fields, including material science, structural engineering, and oil and gas reservoir engineering. A major step in analyzing cracked bodies is the accurate computation of fracture mechanics parameters such as the J-integral and intensity factors (SIFs). It is well known that the SIFs characterize the stress state adjacent to the crack in the context of linear elastic fracture mechanics (LEFM), and therefore their accurate determination is of great importance. SIFs can be calculated analytically or experimentally only for a few geometrical configurations and boundary conditions, and the use of numerical techniques such as the finite element (FE) and the boundary element (BE) method is required for more complicated crack problems. Unlike the FE method, which utilizes discretization of the problem domain, the BE method does not require the region outside of the crack to be meshed. However, the underlying theory of the BE method is much more difficult, and in part for this reason, the use of the FE method in fracture mechanics has gained great popularity. It is generally known that the finite element method can be directly applied to solve any solid mechanics boundary value problem. However, a major difficulty in the use of FE to analyze crack problems lies in capturing the high stress gradients near the crack, and accurately computing the singular stress fields.

The use of FE method to solve fracture mechanics problems attracted great attention in early 1970s when poor results of the FE solutions of crack problems by conventional elements were identified. This was due to the fact that conventional finite elements employ polynomials to interpolate field variables in the domain, and therefore they are not able to reproduce the singular crack tip fields. Significant development of the FE analysis of crack problems was made by Barsoum (1976) and Henshell and Shaw (1975) who independently showed that the singularity at the crack tip can be properly modeled by placing the mid-side node near the crack tip at the quarter-point position. This shift simply results in a nonlinear mapping between the natural and local coordinate systems in a way that a singular strain at the crack tip occurs, and an inverse square root singu-

larity is modeled throughout the element. The element types collapsed quarter-point hexahedrals, quarter-point pentahedrals, and quarter-point bricks have been mostly employed in the last three decades for modeling 3D fractures. The use of these types of elements relies upon the generation of a fully structured mesh around the 3D crack front, which is a difficult and cumbersome task for complex crack configurations. Quarter-point tetrahedral elements can also be used to model the singular fields in the vicinity of crack front (Rajaram et al., 2000; Paluszny and Zimmerman, 2011). Unlike the other types of quarter-point elements, quarter-point tetrahedrals can be used in a fully unstructured and arbitrary mesh layout, such as are required to mesh dense three-dimensional fracture patterns.

In terms of meshing schemes used in analyzing crack bodies and simulating fracture growth in crack propagation tools, there have mainly been three methodologies. The first employs pure hexahedral elements to discretize the whole domain. This methodology has been widely accepted and used for simple geometries. Hexahedral elements are advantageous because: (i) collapsed quarter-point hexahedrals have proven to accurately reproduce the singular fields near the crack, and (ii) straightforward algorithms such as domain integral methods are available to extract the J-integral and stress intensity factors from the FE solutions by hexahedrals. However, the approach requires a fully structured mesh, not only in the neighborhood of the crack front, but also in regions remote from cracks. It is known that meshing an arbitrary crack geometry with hexahedrals is very difficult and cumbersome, and for complex crack and body configurations it may not be feasible. The second methodology employs a combination of hexahedral and tetrahedral elements. These combined methodologies are developed to utilize the good performance of collapsed quarter-point hexahedral finite elements as well as the efficiency of the tetrahedral elements to mesh complicated geometries. One approach is to discretize the neighborhood region of the crack by hexahedrals, while tetrahedrals are used to generate unstructured mesh in the remote regions (Bremberg and Dhondt, 2008, 2009; Bremberg and Faleskog, 2015). The major drawback is that tie constraints must be used to satisfy the compatibility and equilibrium conditions at the surfaces where tetrahe-

drals connect to hexahedrals. In the other approach one analysis is performed to model the global structure by tetrahedrals, and then by mapping the FE-solution, a sub-model is generated to solve for the near crack fields using hexahedrals (Schöllmann et al., 2003). This approach is also computationally expensive, as it requires performing two FE model analyzes, and also, complications may arise in sub-modeling procedures. The third methodology is to use pure tetrahedrals in an unstructured and arbitrary mesh to model the entire domain. This methodology has been successfully applied in the context of crack propagation (Paluszny and Zimmerman, 2011) as well as fragmentation (Paluszny et al., 2013). It is well known that the meshing procedures by tetrahedrals are much simpler, and these elements are best suited to mesh arbitrary domains and complicated geometries automatically. Additionally, adaptive meshing procedures can be applied to discretize the domain efficiently. However, the applicability, efficiency, and accuracy of tetrahedral elements for modeling crack singular fields have not been well investigated in the literature.

Existing methods to extract J-integrals and SIFs using tetrahedral elements are complex and suffer from oscillations (Červenka and Saouma, 1997; Rajaram et al., 2000; Paluszny and Zimmerman, 2011), while others require very fine meshes near the crack front, rely on complicated numerical procedures, and are applied on arbitrary domain shapes and sizes (Okada et al., 2008; Daimon and Okada, 2014). These methods mainly rely on volumetric actual (Rajaram et al., 2000; Daimon and Okada, 2014) and virtual (Červenka and Saouma, 1997; Paluszny and Zimmerman, 2011) domains to compute the SIFs from the evaluated J- and interaction integrals. The present paper proposes an efficient, accurate and straightforward disk-shaped domain integral method to extract J-integral and SIFs from unstructured meshes. This method does not require a very fine mesh near the crack front, and no oscillation is seen in the computed pointwise fracture parameters.

2. Volumetric domain integral method

Techniques for SIF computation from FE results fall into two categories. (i) Direct approaches, such as stress/displacement extrapolation and correlation, which are based on the correlation be-

tween the FE stress/displacement distribution around the crack and the analytical field expressions. Displacement extrapolation method proposed by Chan et al. (1970), displacement correlation approach suggested by Barsoum (1976) and further developed by Shih et al. (1976); Ingraffea and Manu (1980), as well as recently developed least-square based finite element over-deterministic method (FEOD) by Ayatollahi and Nejati (2011a,b) fall into this category. (ii) Energy approaches which are based on the computation of energy released rate $\mathcal{G}$ (Irwin, 1956). The SIFs are then computed indirectly by using the relationships between $\mathcal{G}$ and the SIFs. In the context of LEFM, three main methods have been proposed to compute $\mathcal{G}$: 1) the J-integral: J, which is equivalent to $\mathcal{G}$ for elastic materials, is defined as a contour integral around the crack tip (Cherepanov, 1967; Rice, 1968; Budiansky and Rice, 1973). DeLorenzi (1982) and Li et al. (1985) then transformed this contour integral into an equivalent domain integral. 2) Virtual crack extension: VCE was suggested by Parks (1974), and computes the rate of the change of the total potential energy of the system, for a small virtual extension of the crack. This technique is mathematically equivalent to the domain version of J-integral, and can be interpreted as a virtual crack extension technique (DeLorenzi, 1982; Shih et al., 1986; Banks-Sills and Sherman, 1992; Banks-Sills, 2010). 3) Virtual crack closure technique: VCCT was originally proposed by Rybicki and Kanninen (1977) and uses Irwin's crack closure integral to compute the SIFs. Recently a strain energy based approach has been suggested for the computation of the SIFs of cracks and V-shaped notches from coarse meshes (Lazzarin et al., 2008, 2010; Treifi and Oyadiji, 2013). This method averages strain energy density over a control volume near the crack and notch tips, and uses close form relations to obtain SIFs from the computed averaged strain energy density. This approach is more suitable for pure modes as the decoupling process in mixed-mode configurations is not straightforward.

The J-integral has been the most used crack tip parameter in fracture mechanics, and plays an important role in linear and nonlinear fracture mechanics. Under pure modes I, II or III, the extraction of SIFs from the J-integral is straightforward. However, a technique is required to separate SIFs due to different deformation modes in a mixed-mode crack deformation, as the J-integral

gives the total energy release rate. There have been two main strategies for separating the SIFs. The first strategy uses decomposed crack tip fields to compute separate energy release rates for different deformation modes (Bui, 1983). This approach has been frequently used along with the domain representation of the J-integral for the computation of SIFs (Raju and Shivakumar, 1990; Shivakumar and Raju, 1992; Nikishkov and Atluri, 1987b; Huber et al., 1993). However, decomposing the crack tip field into symmetric and antisymmetric fields introduces error, and is mainly applicable to a mesh that is symmetric with respect to the crack face. The second method is called the interaction integral method, which was initially developed for 2D cracks by Chen and Shield (1977) and Yau et al. (1980), and then extended to 3D crack configurations by Nakamura and Parks (1989). In this method the contribution of the interaction of two different stress fields, a real field and an auxiliary field, to the J-integral defines a new integral which is able to compute separate SIFs. Interaction integral methods have emerged as the most accurate and readily implementable approach to extract SIFs in mixed-mode crack deformation. This section discusses the available domain integral approaches of computing J-integral and interaction-integral from FE results.

2.1. J-integral

Let us consider a two-dimensional elastic body containing a crack which lies in the direction of x_1 as shown in Fig. 1. Restricting the crack to advance along the x_1 axis, the energy release rate per unit crack advance, $\mathcal{G}$, is equivalent to the J-integral (Rice, 1968; Shih et al., 1986):

$$\mathcal{G} = J = \lim_{\Gamma \to 0} \int_{\Gamma} \Big(W\delta_{1i} - \sigma_{ij} \frac{\partial u_j}{\partial x_1} \Big) n_i d\Gamma = \lim_{\Gamma \to 0} \int_{\Gamma} P_{1i} n_i \mathrm{d}\Gamma \tag{1}$$

where $W = \int_0^{\epsilon} \sigma_{ij}\epsilon_{ij} d\epsilon$ is the strain energy density, σ_{ij}, ϵ_{ij} and u_i are the Cartesian components of stress tensor, strain tensor and displacement vector in the local x_1x_2 coordinate system, respectively, δ_{ij} is the Kronecker delta, and n_i is the unit vector normal to Γ which is an arbitrary path beginning at the bottom crack face and ending on the top face. $\Gamma \to 0$ indicates that the contour Γ is shrinking onto the crack tip. The bracketed quantity is in fact the x_1 component of Eshelby's

energy-momentum tensor $P_{1i} = W\delta_{1i} - \sigma_{ij}\partial u_j/\partial x_1$ (Eshelby, 1970). In the absence of body force and thermal strains, the energy density W does not depend explicitly on the system coordinates, and the divergence of P_{1i} vanishes ($P_{1i,i} = 0$). Assuming that the vector m is normal to a closed contour $\Gamma_c = \Gamma_0 + \Gamma_+ + \Gamma_- - \Gamma$ such that $m = -n$ on Γ, $m = n$ on Γ_0, $m_2 = -1$ on Γ_+ , and $m_2 = 1$ on Γ_-, then according to the divergence theorem the integral in Eq. (1) vanishes for Γ_c, $\int_{\Gamma_c} P_{1i}m_i \mathrm{d}\Gamma = 0$, and the J-integral can be expressed as

$$J = \int_{\Gamma_0} \Big(W\delta_{1i} - \sigma_{ij}\frac{\partial u_j}{\partial x_1}\Big)n_i \mathrm{d}\Gamma - \int_{\Gamma_+ + \Gamma_-} \sigma_{2j}\frac{\partial u_j}{\partial x_1} m_2 \mathrm{d}\Gamma \tag{2}$$

Eq. (2) indicates that in the absence of body force and thermal strains, the J-integral is path-independent as long as the contribution of crack face tractions is considered. In fact, the J-integral does not depend on a limiting process in which the crack tip contour Γ is shrunk onto the crack tip, and can be accurately extracted from contours remote from the crack tip. This formulation allows one to use contours remote from the crack tip, which results in the computation of more accurate values for J-integral. However, the evaluation of counter integrals in Eq. (2) is cumbersome in the FE scheme as the contour is preferably selected to pass through Gauss points where stresses are expected to be the most accurate. To circumvent this difficulty, the line-integral form of J can be recast as a domain integral (DeLorenzi, 1982; Li et al., 1985). Let us assume q is a sufficiently smooth scalar function in the region enclosed by $\Gamma_c = \Gamma_0 + \Gamma_+ + \Gamma_- - \Gamma$, holding unity on Γ and vanishing on Γ_0. Eq. (1) can be rewritten as

$$J = \int_A \Big(\sigma_{ij}\frac{\partial u_j}{\partial x_1} - W\delta_{1i}\Big)\frac{\partial q}{\partial x_i} \mathrm{d}A - \int_{\Gamma_+ + \Gamma_-} \sigma_{2j}\frac{\partial u_j}{\partial x_1} m_2 q \mathrm{d}\Gamma \tag{3}$$

where the closed contour integral is transformed to an equivalent domain integral by applying the divergence theorem and making use of the relation ($P_{1i,i} = 0$). Thanks to the scalar function q, the contour integrals in Eq. (2) is now transformed to an area integral over A together with contour integrals over the crack faces. The process of recasting the contour integral into an area integral

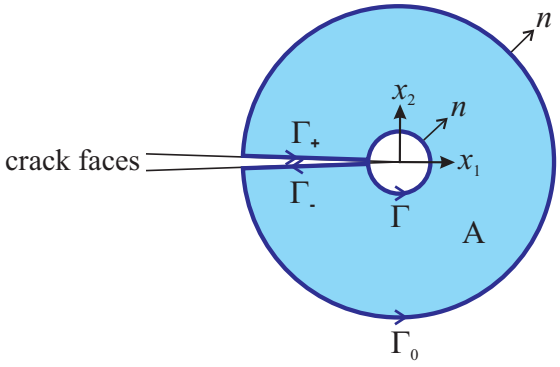

Figure 1: Contour and domain integrals for the evaluation of J-integral in 2D cracks.

is advantageous for numerical purposes, as a domain integral is compatible with the finite element formulations and can be readily implemented in FE codes. Also as the integral is evaluated over a domain of elements surrounding the crack, errors in local solution parameters have less effect on the evaluated quantity of J-integral. It has been shown that the domain version of the J-integral has superior path independence than does the line integral, yielding much more accurate results for the crack field parameters (Nikishkov and Atluri, 1987a; Raju and Shivakumar, 1990). The domain integral method corresponds to a continuum formulation of the finite-element virtual crack extension technique (DeLorenzi, 1982). One can refer to Moran and Shih (1987a,b) for a general discussion on crack-tip contour integrals and their associated domain integral representation.

For a 3D crack configuration, the J-integral generalizes to a surface integral where two definitions of J-integral have been proposed: (i) the average value which gives the average of the energy release rate per unit crack advance at the whole crack front; and (ii) the pointwise value which gives the energy release rate due the extension of the crack front locally at a given point on the crack front (Budiansky and Rice, 1973; DeLorenzi, 1982; Li et al., 1985). The pointwise J-integral reveals the variation of the strength of the energy release rate along the crack front, and can be used to compute the SIFs at any point on the crack front. Consider point s on the curved crack front of a 3D planar crack. A local orthogonal coordinate system is defined at point s such that the local x_2 axis is perpendicular to the plane of the crack, and the x_1, and x_3 axes are normal

and tangent to the crack front, respectively (Fig. 2). The pointwise energy release rate due to the unit local crack advancement at the point s is given by

$$J(s) = \lim_{\Omega \to 0,\, L_c \to 0} \frac{1}{L_c} \int_{\Omega} P_{1i} n_i \mathrm{d}\Omega = \lim_{\Gamma \to 0} \int_{\Gamma} P_{1i} n_i \mathrm{d}\Gamma \tag{4}$$

where Γ is a contour that lies on a plane passing through point s and is perpendicular to the crack front, Ω is the surface of a tube connecting the top and bottom crack faces, and n_i is the unit vector normal to Ω. $\Omega \to 0$ indicates that the surface Ω is shrinking onto the crack front segment L_c. Although the shape of surface Ω may be arbitrary as it collapses onto the crack front, an equivalent path independent integral such as Eq. (2) does not exist for 3D cracks. This is because the two-dimensional plane strain fields are only asymptotically approached at the crack front, and a general 3D state of stress prevails far from the crack front (Nakamura and Parks, 1989). Therefore, for the J-integral to capture the effects of plane strain conditions, the surface must be very close to the crack front. Furthermore, if the surface Ω that is used for the J-integral is too large, then it is influenced by singular fields from other points of the crack front and not just the position of interest (Shivakumar and Raju, 1992; Rigby and Aliabadi, 1998). The presence of two limits and integration over surface make it very cumbersome and error-prone to evaluate the J-integral from its original definition in Eq. (4). However, two steps can be taken to recast the integral into a more compatible formulation within the FE context. In the first step it is assumed that $J(s)$ varies slowly over a small segment of the crack front L_c which has undergone a crack advancement of $\delta l(s)$, and reformulate Eq. (4) as

$$J(s) = \frac{1}{\int_{L_f} \delta l(s) \mathrm{d}s} \lim_{\Omega \to 0} \int_{\Omega} P_{1i} \delta l(s) n_i \mathrm{d}\Omega \tag{5}$$

where the crack advance $\delta l(s)$ is continuously differentiable arbitrary function that equals zero at the two ends of L_c (Fig. 2). The second step is to recast the surface integral into a domain integral version. Consider a tubular domain V surrounding the crack segment L_c, which is enclosed by the

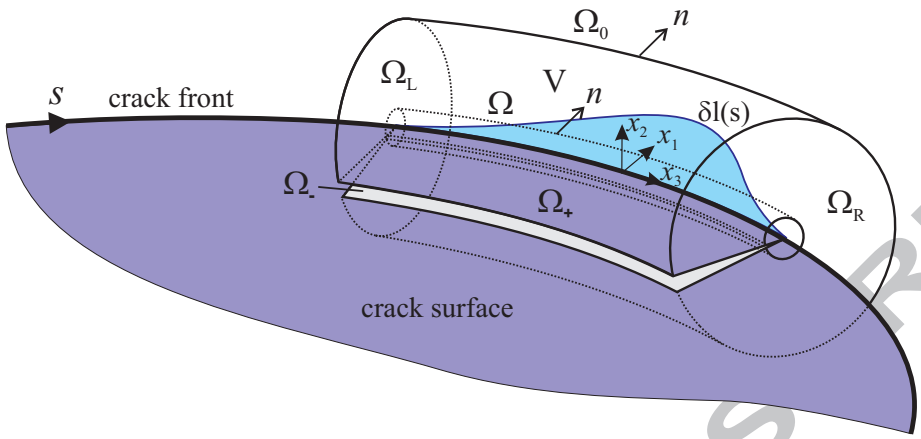

Figure 2: The tubular domain V surrounding the crack segment L_c, which is enclosed by the closed manifold $\Omega_c = \Omega + \Omega_0 + \Omega_L + \Omega_R + \Omega_+ + \Omega_-$ where Ω shrinks onto the crack front.

closed manifold $\Omega_c = \Omega + \Omega_0 + \Omega_L + \Omega_R + \Omega_+ + \Omega_-$ with the outward-point normal vector m where $m = -n$ on Ω, $m = n$ on Ω_0, $m_2 = -1$ on Ω_+ and $m_2 = 1$ on Ω_- (see Fig. 2). These surfaces are formed by translating the contour Γ, Γ_0, Γ_+ and Γ_- in Fig. 1 along the curved crack front segment L_c. Now introduce an arbitrary continuously differentiable, class C^1, scalar function q in the neighborhood of V, which is equal to $\delta l(s)$ on the surface Ω, and zero on Ω_0, Ω_R and Ω_L. Applying the divergence theorem, and knowing that in the absence of thermal strains and body forces, and when the equilibrium conditions are satisfied throughout the whole domain V ($\partial\sigma_{ij}/\partial x_j = 0$), P_{1i} is divergence free ($\partial P_{1i}/\partial x_i = 0$), Eq. (5) is reformulated to

$$J(s) = \frac{1}{\int_{L_c} q(s)\mathrm{d}s}\left[\int_V \left(\sigma_{ij}\frac{\partial u_j}{\partial x_1} - W\delta_{1i}\right)\frac{\partial q}{\partial x_i}\mathrm{d}V - \int_{\Omega_+ + \Omega_-} \sigma_{2j}\frac{\partial u_j}{\partial x_1} m_2 q \mathrm{d}\Omega\right] \tag{6}$$

By separately advancing various small segments of the crack front, the pointwise J-integral can be computed along the crack front (Shih et al., 1986; Nikishkov and Atluri, 1987b; Shivakumar and Raju, 1992). Volume integration is performed over a volumetric domain around the crack front; a special concentric mesh is required to define a structured domain around the crack front.

2.2. Interaction integral to extract stress intensity factors

The SIFs K_{I}, K_{II}, and K_{III} cannot be calculated separately from the J-integral. The interaction integral, however, is able to extract the separated SIFs from the FE results. Chen and Shield (1977) and Yau et al. (1980) introduced this method for 2D cracks, and Nakamura and Parks (1989) extended it to 3D crack configurations. Interaction integral methods are perhaps the most accurate, reliable and readily implementable methods to extract SIFs in mixed-mode 2D and 3D crack problems (Walters et al., 2005; Banks-Sills, 2010; Bremberg and Faleskog, 2015). Consider two states of equilibrium for the cracked body deformation: (i) an actual state obtained by the FE solution of the actual boundary value problem ($u_i, \epsilon_{ij}, \sigma_{ij}$); and (ii) an auxiliary state given by the known asymptotic fields which are functions of the SIFs ($u_i^{\mathrm{aux}}, \epsilon_{ij}^{\mathrm{aux}}, \sigma_{ij}^{\mathrm{aux}}$). Except at points that are very close to the intersection point of a crack front with free surfaces, the two-dimensional plane strain fields are asymptotically approached at the crack front (Nakamura and Parks, 1988, 1989). Therefore, the first terms of the Williams series expansions for stresses, strains and displacements in 2D cracks are usually chosen as the auxiliary fields in the vicinity of the crack front (Appendix A). A linear combination of actual fields (or finite element fields) with auxiliary fields (field expressions as functions of SIFs) constitutes a third, superimposed, equilibrium state. From Eq. (4), the J-integral for this superimposed equilibrium state is given by

$$J^{\mathrm{sup}}(s) = \lim_{\Gamma \to 0} \int_{\Gamma} \Big[\frac{1}{2} (\sigma_{ij} + \sigma_{ij}^{\mathrm{aux}})(\epsilon_{ij} + \epsilon_{ij}^{\mathrm{aux}}) \delta_{1i} - (\sigma_{ij} + \sigma_{ij}^{\mathrm{aux}}) \Big(\frac{\partial u_j}{\partial x_1} + \frac{\partial u_j^{\mathrm{aux}}}{\partial x_1} \Big) \Big] n_i d\Gamma \tag{7}$$

Consider $J^{\mathrm{sup}}(s) = J^{\mathrm{act}}(s) + J^{\mathrm{aux}}(s) + I(s)$, where $J^{\mathrm{act}}(s)$ and $J^{\mathrm{aux}}(s)$ are the energy release rates due to the actual and auxiliary fields, and $I(s)$ is the interaction integral for the two states of equilibrium. By comparing the energy release rate for the superimposed state with the energy release rates for the separate actual and auxiliary fields, the interaction integral is formulated as

$$I(s) = \lim_{\Gamma \to 0} \int_{\Gamma} \Big[W_{\mathrm{I}} \delta_{1i} - \Big(\sigma_{ij} \frac{\partial u_j^{\mathrm{aux}}}{\partial x_1} + \sigma_{ij}^{\mathrm{aux}} \frac{\partial u_j}{\partial x_1} \Big) \Big] n_i d\Gamma \tag{8}$$

where $W_{\mathrm{I}} = 1/2(\epsilon_{ij}^{\mathrm{aux}}\sigma_{ij} + \epsilon_{ij}\sigma_{ij}^{\mathrm{aux}})$ is the mutual strain density, and as the actual and auxiliary fields provide two solutions for the same elastic solid with the same constitutive tensor, according to the reciprocal theorem $W_{\mathrm{I}} = \epsilon_{ij}^{\mathrm{aux}}\sigma_{ij} = \epsilon_{ij}\sigma_{ij}^{\mathrm{aux}}$. In the context of LEFM, the two very important fracture parameters, namely the energy release rate $\mathcal{G}$, which gives the change in the potential energy that accompanies an increment of crack extension, and the stress intensity factors K_{I}, K_{II} and K_{III}, which characterize the stresses, strains, and displacement near the crack front for different modes, are uniquely related by (Anderson, 2005)

$$\mathcal{G} = J = \frac{K_{\mathrm{I}}^2 + K_{\mathrm{II}}^2}{E'} + \frac{K_{\mathrm{III}}^2}{2\mu} \tag{9}$$

where $E' = E$ and $E' = E/(1-\nu^2)$ for plane stress and plane strain conditions, respectively, and E, ν and $\mu = E/2(1+\nu)$ are the Young's modulus, Poisson's ratio, and shear modulus of the material. As plane strain condition prevails very close to the crack front at any point on the crack front except points very close to the intersection of the crack front and free surfaces (Nakamura and Parks, 1988, 1989), a plane strain condition must be assumed in order to relate $\mathcal{G}(s)$ to the SIFs. Using Eq. (9) the energy release rate for the superimposed state in terms of SIFs will be

$$J^{\mathrm{sup}}(s) = J^{\mathrm{act}}(s) + J^{\mathrm{aux}}(s) + I(s) = \frac{\left(K_{\mathrm{I}}(s) + K_{\mathrm{I}}^{\mathrm{aux}}(s)\right)^2 + \left(K_{\mathrm{II}}(s) + K_{\mathrm{II}}^{\mathrm{aux}}(s)\right)^2}{E'} + \frac{\left(K_{\mathrm{III}}(s) + K_{\mathrm{III}}^{\mathrm{aux}}(s)\right)^2}{2\mu} \tag{10}$$

where $K_{\mathrm{I}}(s)$, $K_{\mathrm{II}}(s)$ and $K_{\mathrm{III}}(s)$ are the SIFs due to the actual state, and $K_{\mathrm{I}}^{\mathrm{aux}}(s)$, $K_{\mathrm{II}}^{\mathrm{aux}}(s)$ and $K_{\mathrm{III}}^{\mathrm{aux}}$ are the SIFs due to the auxiliary states. The interaction energy integral is then developed in terms of SIFs as

$$I(s) = \frac{2}{E'}\Big(K_{\mathrm{I}}(s)K_{\mathrm{I}}^{\mathrm{aux}}(s) + K_{\mathrm{II}}(s)K_{\mathrm{II}}^{\mathrm{aux}}(s)\Big) + \frac{1}{\mu}K_{\mathrm{III}}(s)K_{\mathrm{III}}^{\mathrm{aux}}(s) \tag{11}$$

By using following three equilibrium auxiliary states of pure mode I $(K_{\mathrm{I}}^{\mathrm{aux}}, K_{\mathrm{II}}^{\mathrm{aux}}, K_{\mathrm{III}}^{\mathrm{aux}}) =$

$(1,0,0)$, pure mode II $(K_{\mathrm{I}}^{\mathrm{aux}}, K_{\mathrm{II}}^{\mathrm{aux}}, K_{\mathrm{III}}^{\mathrm{aux}}) = (0,1,0)$, and pure mode III $(K_{\mathrm{I}}^{\mathrm{aux}}, K_{\mathrm{II}}^{\mathrm{aux}}, K_{\mathrm{III}}^{\mathrm{aux}}) = (0,0,1)$, three corresponding interaction integral values $I_{\mathrm{I}}(s)$, $I_{\mathrm{II}}(s)$ and $I_{\mathrm{III}}(s)$ are obtained from Eq. (8), and the SIFs are extracted from the following expressions:

$$K_{\mathrm{I}}(s) = \frac{E'}{2} I_{\mathrm{I}}(s), \quad K_{\mathrm{II}}(s) = \frac{E'}{2} I_{\mathrm{II}}(s), \quad K_{\mathrm{III}}(s) = \mu I_{\mathrm{III}}(s) \tag{12}$$

Equation (8) is not in a form well suited for finite element calculations. The same approach that was used in Section 2.1 can be used to recast this integral into a domain integral, which is more compatible with the context of finite elements. Again consider the tubular domain V surrounding the crack segment L_c, which is enclosed by the closed manifold Ω_c, with the outward-point normal vector m, and also consider the scalar function q as explained in Section 2.1 (Fig. 2). Applying the divergence theorem, Eq. (8) is reformulated to

$$\begin{aligned} I(s) = \frac{1}{\int_{L_c} q(s)\mathrm{d}s} \Bigg[& \int_V \left(\sigma_{ij} \frac{\partial u_j^{\mathrm{aux}}}{\partial x_1} + \sigma_{ij}^{\mathrm{aux}} \frac{\partial u_j}{\partial x_1} - W_{\mathrm{I}} \delta_{1i} \right) \frac{\partial q}{\partial x_i} \mathrm{d}V \\ & + \int_V \left(\sigma_{ij} \frac{\partial}{\partial x_1} \left(\frac{\partial u_j^{\mathrm{aux}}}{\partial x_i} - \epsilon_{ij}^{\mathrm{aux}} \right) + \frac{\partial \sigma_{ij}^{\mathrm{aux}}}{\partial x_i} \frac{\partial u_j}{\partial x_1} \right) q \mathrm{d}V \\ & - \int_{\Omega^+ + \Omega^-} \sigma_{2j} \frac{\partial u_j^{\mathrm{aux}}}{\partial x_1} m_2 q \mathrm{d}\Omega \Bigg] \end{aligned} \tag{13}$$

Equation (13) is derived for isothermal loading without body forces, assuming that in the actual state the equilibrium and compatibility conditions are satisfied throughout the entire domain V ($\partial \sigma_{ij}/\partial x_j = 0, \partial u_j/\partial x_i - \epsilon_{ij} = 0$). For a straight crack front, the 2D plane strain auxiliary fields also satisfy compatibility and equilibrium equations, and therefore, the second integral in Eq. (13) vanishes. In the case of curved crack fronts, however, special care must be taken, as Williams 2D plane strain auxiliary fields do not satisfy compatibility ($\partial u_j^{\mathrm{aux}}/\partial x_i - \epsilon_{ij}^{\mathrm{aux}} \neq 0$) and equilibrium ($\sigma_{ij}^{\mathrm{aux}}/\partial x_i \neq 0$) in curvilinear coordinates and the second integral remains non-zero (Nahta and Moran, 1993; Gosz et al., 1998; Gosz and Moran, 2002). The main difficulty in calculating the

interaction energy integral from the domain form in Eq. (13) lies in the evaluation of the gradients and higher order gradients of the auxiliary fields that appear in the second integrand in Eq. (13). Nahta and Moran (1993); Gosz et al. (1998) presented a method to evaluate this integral by introducing curvilinear coordinates in the definition of deformation gradients. Kim et al. (2001) proposed a method to calculate the two-state integral in Eq. (13) through imposing displacement of the two dimensional asymptotic solutions on the nodes in the finite element model. Both methods involve the computation of highly accurate values of the coordinates of the integration points with respect to the curved crack front, which usually require a Newton scheme and an analytical definition for the local crack front geometry. Walters et al. (2005) proposed another strategy in which elements with straight edges are used along the crack front. This approach eliminates this additional integral appearing in the interaction integral formulation for curvilinear coordinates. It has been demonstrated that it is crucial to maintain this integrand, especially when the local crack front curvature is high (Gosz et al., 1998; Kim et al., 2001). The third terms in Eq. (13) also involves the evaluation of surface integrals, which include singular terms. An accurate evaluation of this integral ensures that it does not contribute numerical error to the SIF results.

The existing volumetric domain integral approaches use Eqs. (6) and (13) to evaluate the J-integral and interaction integrals, respectively. As they evaluate integrals over tubular domains built by a set of volumetric elements, a structured mesh is required around the crack front. The main advantage of these versions of domain integrals is that they can be readily implemented in the FE codes when a structured mesh is used near the crack front. The main disadvantages of these forms are: (i) Implementation of these methods on an unstructured mesh is very cumbersome; (ii) The method requires the crack tip fields to be obtained in a curvilinear coordinate system by the computation of accurate values of the coordinates of the integration points with respect to the curved crack front, which usually requires a Newton scheme and an analytical definition for the local crack front geometry; (iii) The computation of the second integral in Eq. (13) requires computation of the higher-order gradients of crack tip fields, which is not trivial. The question

arises as to whether this is the best domain form choice to be used in the case of an unstructured mesh around the crack front.

3. Disk-shaped domain integral approach

Consider a cracked body under mechanical loading only, in the absence of any body force. The arbitrarily-shaped planar crack is assumed to lie in a plane described by $X_p(X_1, X_2, X_3) = 0$ whose crack front is of length L_f, as shown in Fig. 3. The crack front is a smooth plane curve that is described by the position vector $X_f(s)$, where $0 \leq s \leq L_f$ parameterizes the points along the crack front. The unit normal vector to the crack surface is constant ($N_p = \nabla X_p / \|\nabla X_p\|$), but the unit tangent vector to the crack front will be a function of s ($T(s) = X_f'(s)/\|X_f'(s)\|$). The unit normal to the crack front which lies in the crack plane and is in the direction of crack extension is also a function of s and is defined by $N_f(s) = N_p \times T(s)$. A right-handed orthogonal curvilinear coordinate system $x_1 x_2 x_3$ is constructed in a way that the x_3 axis coincide with the curved crack front. In this coordinate system, $x_3 = s$ indicates a plane normal to the crack front, and the local unit base vectors at the point s along the crack front are $b_1 = N_f(s)$, $b_2 = N_p$, and $b_3 = T(s)$.

3.1. J-integral

Assume a virtual crack advance of $\delta l(s) = \delta(x_3 - s) b_1$ in the curvilinear coordinate system $x_1 x_2 x_3$. Here $\delta(x_3 - s)$ is the Dirac delta function, which is zero along the crack front except at the point s, and gives a pointwise crack extension at the point s on the crack front. Due to this virtual crack extension, the negative of the change of the potential energy of the body (Π) is equivalent to the pointwise energy release rate:

$$-\delta\Pi = \int_0^{L_f} \mathcal{G}(x_3)\delta(x_3 - s)\mathrm{d}x_3 = \mathcal{G}(s) \tag{14}$$

Equation (14) implies that the Dirac delta function is a proper choice for the virtual crack extension in order to evaluate the pointwise energy release rate as the unit crack extension occurs

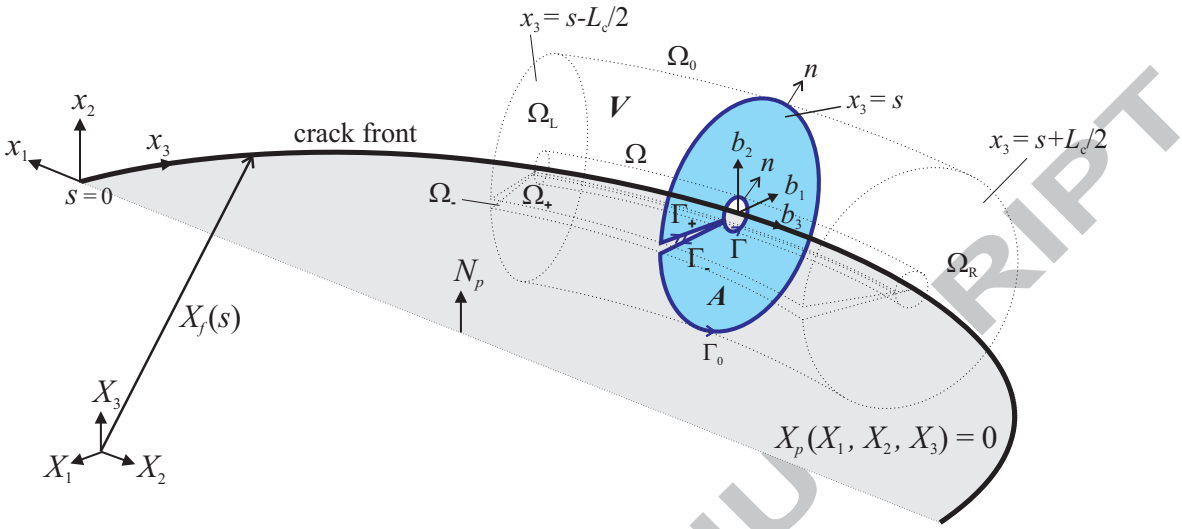

Figure 3: Disk-shaped domain for the evaluation of J- and interaction integrals in 3D crack configurations.

at the point s only, remaining elsewhere at its original length. Now consider an arbitrary path Γ beginning at the bottom crack face and ending on the top face, with n_i being its unit normal vector (Fig. 3). Both contour path Γ and its normal n_i lie in the plane $x_3 = s$, which is normal to the crack front at the point s. The tubular surface Ω is now formed by translating the contour Γ along the curved crack front segment L_c (Fig. 3). From Eq. (4), the pointwise energy release rate $\mathcal{G}$ is equivalent to the well-known J-integral:

$$\mathcal{G}(s) = J(s) = \lim_{\Gamma \to 0} \int_{\Gamma} P_{1i} n_i \mathrm{d}\Gamma = \lim_{\Omega \to 0} \int_{\Omega} P_{1i} n_i \delta(x_3 - s) \mathrm{d}\Omega \tag{15}$$

where $\Gamma \to 0$ and $\Omega \to 0$ indicate that the contour Γ and the surface Ω are shrinking down to the point $x_3 = s$, and crack segment L_c, respectively. Let us consider a tubular domain V surrounding the crack segment L_c, which is enclosed by the closed manifold $\Omega_c = \Omega + \Omega_0 + \Omega_L + \Omega_R + \Omega_+ + \Omega_-$ with the outward-point normal vector m where $m = -n$ on Ω, $m = n$ on Ω_0, $m_2 = -1$ on Ω_+ and $m_2 = 1$ on Ω_- (see Fig. 3). These surfaces are formed by translating the enclosed contour $\Gamma_c = \Gamma_0 + \Gamma_+ + \Gamma_- - \Gamma$ at the plane $x_3 = s$ along the curved crack front segment L_c. Let us also

introduce an arbitrary continuously differentiable scalar function $q(x_1, x_2)$, which is equal to unity on Ω, and zero on Ω_0. $q(x_1, x_2)\delta(x_3 - s)$ is therefore a continuously differentiable scalar function which is equal to $\delta l(x_3) = \delta(x_3 - s)$ on Ω, and zero on Ω_0. In the absence of thermal strains and body forces, and when the equilibrium conditions are satisfied throughout the whole domain A ($\partial\sigma_{ij}/\partial x_j = 0$), P_{1i} is divergence-free on A ($\partial P_{1i}/\partial x_i = 0$). Applying the divergence theorem, the surface integral in Eq. (15) is reformulated to a domain integral as

$$J(s) = \int_A \Big(\sigma_{ij}\frac{\partial u_j}{\partial x_1} - W\delta_{1i}\Big)\frac{\partial q}{\partial x_i}\mathrm{d}A - \frac{\partial}{\partial x_3}\int_A \sigma_{3j}\frac{\partial u_j}{\partial x_1}\, q\mathrm{d}A - \int_{\Gamma^+ + \Gamma^-} \sigma_{2j}\frac{\partial u_j}{\partial x_1} m_2 q \mathrm{d}\Gamma \qquad (16)$$

where A is a disk-shaped area in the plane orthogonal to the crack front at point s, and Γ_+ and Γ_- are the contours on the crack faces with $m_2 = -1$ and $m_2 = 1$, respectively. Here the fundamental equation that defines derivatives of the delta function ($\int f(x)\delta'(x)\mathrm{d}x = -\int f'(x)\delta(x)\mathrm{d}x$) has been used. As 2D plane strain conditions are approached asymptotically near crack tip field, the integration area A must be very close to the crack front. It is noteworthy that $\partial q/\partial x_3 = 0$ as q is a function of only x_1 and x_2. Now consider the following two states of equilibrium superimposed on top of each other over the disk A: (**a**) an equilibrium state generated due to in-plane loads ($u^{\mathbf{a}} = \{u_1, u_2, 0\}^T, \epsilon^{\mathbf{a}} = \{\epsilon_{11}, \epsilon_{22}, \epsilon_{33}, \epsilon_{12}, 0, 0\}^T, \sigma^{\mathbf{a}} = \{\sigma_{11}, \sigma_{22}, \sigma_{33}, \sigma_{12}, 0, 0\}^T$); (**b**) an equilibrium state generated due to anti-plane loads ($u^{\mathbf{b}} = \{0, 0, u_3\}^T, \epsilon^{\mathbf{b}} = \{0, 0, 0, 0, \epsilon_{13}, \epsilon_{23}\}^T, \sigma^{\mathbf{b}} = \{0, 0, 0, 0, \sigma_{13}, \sigma_{23}\}^T$). The actual fields within the area A are obtained by superimposing the states **a** and **b** (see Fig. 4). The state **a** provokes a mixed-mode I/II crack deformation only, while the state **b** can produce mode III deformation only. In fact, neither can state **a** produce mode III deformation ($K_{\mathrm{III}} = 0$ for state **a**), nor is state **b** able to generate in-plane crack deformation ($K_{\mathrm{I}} = K_{\mathrm{II}} = 0$ for state **b**). As a result, the two states are fully decoupled and cannot interact with each other, and therefore the J-integral of the superimposed state is equivalent to the sum of the J-integrals obtained from the fields in states **a** and **b** separately ($J = J^{\mathbf{a}} + J^{\mathbf{b}}$). As the second integral in Eq. (16) vanishes for each of equilibrium states **a** and **b**, the J-integral is simplified to

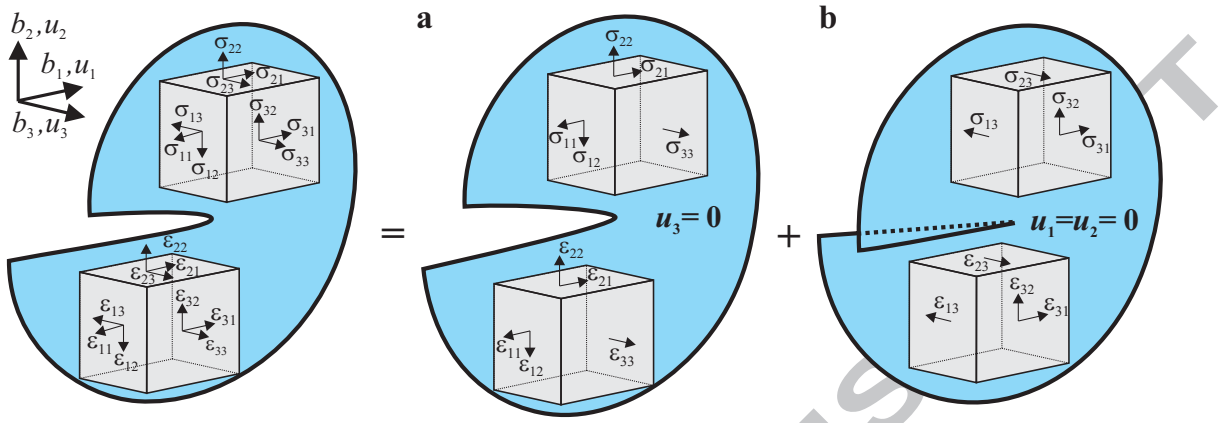

Figure 4: Decomposition of crack tip fields into state **a**: fields from in-plane loads, and state **b**: fields from anti-plane loads.

$$J(s) = \int_A \left(\sigma_{ij}\frac{\partial u_j}{\partial x_1} - W\delta_{1i}\right)\frac{\partial q}{\partial x_i}\mathrm{d}A - \int_{\Gamma^+ + \Gamma^-} \sigma_{2j}\frac{\partial u_j}{\partial x_1} m_2 q \mathrm{d}\Gamma \tag{17}$$

3.2. Interaction integral to extract SIFs

Again assume a virtual crack advance of $\delta l(s) = \delta(x_3 - s)b_1$ in the curvilinear coordinate system $x_1x_2x_3$, and the arbitrary path Γ with unit normal n_i which lies in the plane $x_3 = s$. The tubular surface Ω is formed by translating the contour Γ along the curved crack front segment L_c (Fig. 3). From Eq. (8), and by defining $P'_{1i} = W_1\delta_{1i} - (\sigma_{ij}\partial u_j^{\mathrm{aux}}/\partial x_1 + \sigma_{ij}^{\mathrm{aux}}\partial u_j/\partial x_1)$, the pointwise interaction integral is given by

$$I(s) = \lim_{\Gamma\to 0}\int_\Gamma P'_{1i}n_i\mathrm{d}\Gamma = \lim_{\Omega\to 0}\int_\Omega P'_{1i}n_i\delta(x_3 - s)\mathrm{d}\Omega \tag{18}$$

Again consider a tubular domain V as shown in Fig. 3, and the arbitrary continuously differentiable scalar function $q(x_1, x_2)$ which is equal to unity on Ω, and is zero on Ω_0. $q(x_1, x_2)\delta(x_3 - s)$ is therefore a continuously differentiable scalar function which is equal to $\delta l(x_3) = \delta(x_3 - s)$ on Ω, and is zero on Ω_0. It can be easily shown that $(\partial P'_{1i}/\partial x_i = 0)$ in the whole domain A, since for both actual and auxiliary fields the equilibrium conditions $(\partial\sigma_{ij}/\partial x_j = 0, \partial\sigma_{ij}^{\mathrm{aux}}/\partial x_j = 0)$ and compat-

ibility conditions ($\partial u_j/\partial x_i - \epsilon_{ij} = 0$, $\partial u_j^{\text{aux}}/\partial x_i - \epsilon_{ij}^{\text{aux}} = 0$) are satisfied. Applying the divergence theorem, the surface integral in Eq. (18) is reformulated to a domain integral as

$$I(s) = \int_A \left(\sigma_{ij}\frac{\partial u_j^{\text{aux}}}{\partial x_1} + \sigma_{ij}^{\text{aux}}\frac{\partial u_j}{\partial x_1} - W_{\text{I}}\delta_{1i}\right)\frac{\partial q}{\partial x_i}\mathrm{d}A - \frac{\partial}{\partial x_3}\int_A \left(\sigma_{3j}\frac{\partial u_j^{\text{aux}}}{\partial x_1} + \sigma_{3j}^{\text{aux}}\frac{\partial u_j}{\partial x_1}\right)q\mathrm{d}A - \int_{\Gamma^+ + \Gamma^-} \sigma_{2j}\frac{\partial u_j^{\text{aux}}}{\partial x_1} m_2 q \mathrm{d}\Gamma \tag{19}$$

where A is the disk-shaped domain in the plane orthogonal to the crack front at point s, and Γ^+ and Γ^- are the contours on the crack faces with $m_2 = -1$ and $m_2 = 1$, respectively. Again consider two following states of equilibrium superimposed on top of each other over the very small area A: (**a**) an equilibrium state generated due to in-plane loads ($u^{\mathbf{a}} = \{u_1, u_2, 0\}^T, \epsilon^{\mathbf{a}} = \{\epsilon_{11}, \epsilon_{22}, \epsilon_{33}, \epsilon_{12}, 0, 0\}^T, \sigma^{\mathbf{a}} = \{\sigma_{11}, \sigma_{22}, \sigma_{33}, \sigma_{12}, 0, 0\}^T$); (**b**) an equilibrium state generated due to anti-plane loads ($u^{\mathbf{b}} = \{0, 0, u_3\}^T, \epsilon^{\mathbf{b}} = \{0, 0, 0, 0, \epsilon_{13}, \epsilon_{23}\}^T, \sigma^{\mathbf{b}} = \{0, 0, 0, 0, \sigma_{13}, \sigma_{23}\}^T$). The actual fields within the area A are obtained by superposing the states **a** and **b** (see Fig. 4). The state **a** produces a mixed-mode I/II crack deformation only, while the state **b** can produce mode III deformation only. Consider now the auxiliary fields for mode I as ($u^{\text{aux}} = \{u_1^{\text{aux}}, u_2^{\text{aux}}, 0\}^T, \epsilon^{\text{aux}} = \{\epsilon_{11}^{\text{aux}}, \epsilon_{22}^{\text{aux}}, \epsilon_{33}^{\text{aux}}, \epsilon_{12}^{\text{aux}}, 0, 0\}^T, \sigma^{\text{aux}} = \{\sigma_{11}^{\text{aux}}, \sigma_{22}^{\text{aux}}, \sigma_{33}^{\text{aux}}, \sigma_{12}^{\text{aux}}, 0, 0\}^T$). K_{I} can now be computed by substituting superimposed states and the mode I auxiliary fields in Eq. (19). From the equilibrium states **a** and **b**, only state **a** contributes to the crack deformation in mode I, and the equilibrium state **b** shall be ignored. Considering the auxiliary fields, and equilibrium state **a** only, the second integral in Eq. (19) vanishes. The same logic can be applied for formulating the interaction integral associated with modes II and III to eliminate the second integral in Eq. (19). The interaction integral formulation in Eq. (19) therefore simplifies to

$$I(s) = \int_A \left(\sigma_{ij}\frac{\partial u_j^{\text{aux}}}{\partial x_1} + \sigma_{ij}^{\text{aux}}\frac{\partial u_j}{\partial x_1} - W_{\text{I}}\delta_{1i}\right)\frac{\partial q}{\partial x_i}\mathrm{d}A - \int_{\Gamma^+ + \Gamma^-} \sigma_{2j}\frac{\partial u_j^{\text{aux}}}{\partial x_1} m_2 q \mathrm{d}\Gamma \tag{20}$$

By using the following three equilibrium auxiliary states of pure mode I ($K_{\text{I}}^{\text{aux}}, K_{\text{II}}^{\text{aux}}, K_{\text{III}}^{\text{aux}}$) = (1, 0, 0), pure mode II ($K_{\text{I}}^{\text{aux}}, K_{\text{II}}^{aux}, K_{\text{III}}^{\text{aux}}$) = (0, 1, 0), and pure mode III ($K_{\text{I}}^{\text{aux}}, K_{\text{II}}^{\text{aux}}, K_{\text{III}}^{\text{aux}}$) = (0, 0, 1),

three corresponding interaction integral values $I_{\mathrm{I}}(s)$, $I_{\mathrm{II}}(s)$ and $I_{\mathrm{III}}(s)$ are obtained from Eq. (20), and the SIFs are extracted from Eq. (12).

3.3. Volumetric vs. disk-shaped domain integrals

New versions of domain integrals for computing J- and interaction integrals in 3D cracks were developed in Eqs. (17) and (20). These versions are similar to the domain integral formulations developed for 2D cracks. The main advantage of the volumetric domain integrals is that the domain can be built by a set of elements around the crack front. As a result, the numerical integration is readily implemented using the integration points of the elements. This is a major advantage of the volumetric domain approach, if a structured mesh provides a well-defined tubular region around the crack front. However, for the case of an unstructured mesh where the domain integral is most likely to be independent of the mesh structure, the volumetric domain integral may not be the best option.

The advantages of the disk-shaped domain integrals over the volumetric ones are as follows: (1) They can be readily implemented for unstructured meshes. (2) They directly use the original definition of the pointwise J integral and interaction integrals in Eqs. (4) and (8) without using any approximation. This is not the case in the volumetric domain integrals, where an error may arise from the assumption of the small variation of fracture parameters along the local crack segment L_c. (3) The new versions perform the integration over a disk perpendicular to the crack front, and therefore determining the position of the integration points with respect to the curved crack front is very simple. In fact, in these domains, expressing the stress, strain and displacement fields in a curvilinear coordinate system is no longer required. This is not the case for the volumetric domains, where expressing the fields in a curvilinear coordinate system requires determining the position of integration points with respect to a curved crack front, which is usually performed by minimizing the distance of the integration point from the crack front through a Newton procedure. (4) As the 2D plane strain auxiliary fields do not satisfy the compatibility and equilibrium equations in the curvilinear coordinates, a new term containing the higher order

gradients of the auxiliary fields emerges in the volumetric domain integral formulation (the second term in Eq. (13)). In the disk-shaped domain integral formulation, however, such a term does not exist as the 2D plane strain auxiliary fields satisfy the compatibility and equilibrium equations throughout a disk-shaped domain. (5) The new formulation requires less computational cost, as it performs integration over a disk rather than a tube. Moreover, unlike the volumetric approach, the disk-shaped domain integrals do not require performing iterative procedures to obtain the fields in curvilinear coordinates, which significantly reduces computational effort. (6) In the disk-shaped domain integral, the in-plane and anti-plane fields are separated, and cannot influence each other in the computation of fracture parameters. In fact, the in-plane numerical results cannot affect the computation of out-of-plane mode III stress intensity factor, and anti-plane numerical fields cannot also influence the computation of in-plane mode I and II stress intensity factors.

4. Finite element implementation details

New formulations for the evaluation of pointwise J- and interaction integrals using disk-shaped domains were presented in Section 3. As this type of domain cannot be represented by a set of volumetric elements, the existing elements cannot be directly used in the integration process. A novel, efficient and accurate approach for the evaluation of domain integrals, based on using a set of virtual triangular and line elements, is now presented. In this approach, the disk-shaped domain A is filled with virtual quadratic triangular elements, while the contours on the crack surfaces, Γ_- and Γ_+, are discretized by line elements (see Fig. 5). These elements are referred to as *virtual* since they are not used while performing the finite element solution of the boundary value problem. In fact, these elements are constructed in the post-processing stage, and discarded after the domain integrals are evaluated at the point s along the crack front. The presented domain integration can be readily implemented in any FE code. Moreover, these virtual elements make the process of integrating over the domain completely independent of the mesh structure and resolution around the crack front. This is a great advantage, as accurate domain integrals can be evaluated by using

fine virtual elements, although a coarse mesh discretization may have been used for the finite element solution.

Consider a point s along the crack front with the local coordinate system $x_1x_2x_3$. Due to the domain symmetry, only one-quarter of the disk of radius R_d is discretized with virtual triangular elements, and the contour Γ_+ is discretized by line elements. The integration over the other three quarters is readily evaluated by the reflection of integrating points of the generated virtual elements (see Fig. 5). Quarter-point tetrahedrals reproduce square root singular ($1/\sqrt{r}$) fields in the vicinity of the crack front; therefore, evaluation of area integrals in Eqs. (17) and (20) requires numerical integration of singular integrands of type $1/r$. Standard Gauss-quadrature integration scheme performs well only when the integrand varies gradually; in fact, the use of standard quadrature rules to compute the integration of singular functions results in significant errors unless the domain is subdivided into many subdivisions. Here it is proposed that the mid-side nodes of the virtual triangular/bar elements attached to the crack front be moved to the quarter-point position (see Fig. 5). These quarter-point virtual elements significantly improve the accuracy of the numerical integration, as the determinant of Jacobian matrix cancels out the singular terms in the integrands (see Appendix B for more explanation). It is noteworthy that these virtual quarter-point triangular elements have to be used only when quarter-point tetrahedral elements have been employed in the FE solution; virtual standard triangular elements would suffice when standard tetrahedral elements are used in the vicinity of the crack front.

Using the virtual elements, evaluation of the domain integrals in Eqs. (17) and (20) follows the same standard Gauss-quadrature integration scheme available in any FE code:

$$J(s) = \sum_{A}^{\text{elems}} \sum_{p}^{\text{gpts}} \left\{ \left[\left(\sigma_{ij} \frac{\partial u_j}{\partial x_1} - W\delta_{1i} \right) \frac{\partial q}{\partial x_i} \right] |\mathbf{J}| \right\}_p w_p - \sum_{\Gamma_-+\Gamma_+}^{\text{elems}} \sum_{p}^{\text{gpts}} \left[\left(\sigma_{2j} \frac{\partial u_j}{\partial x_1} m_2 q \right) |\mathbf{J}| \right]_p w_p \tag{21}$$

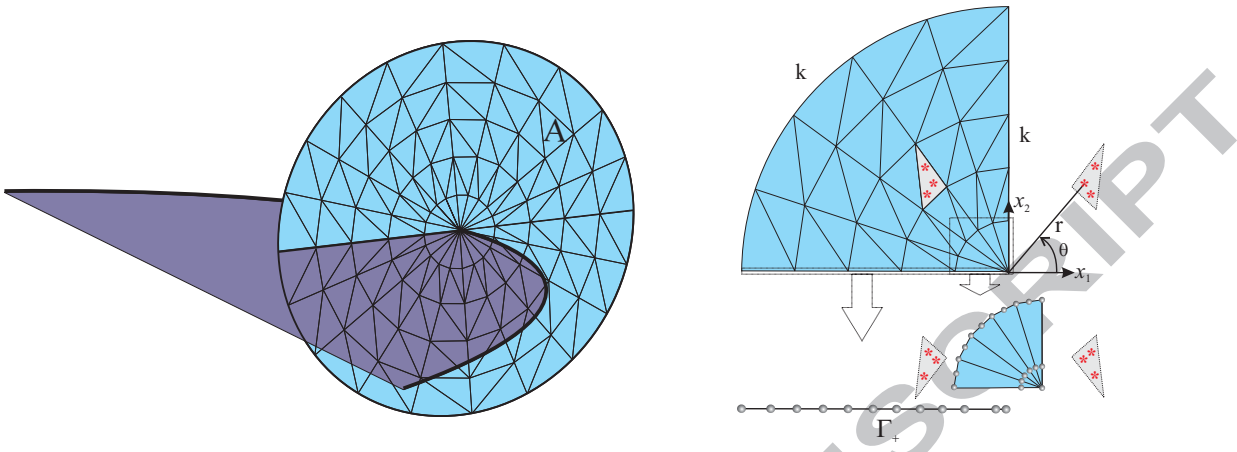

(a) (b)

Figure 5: (a) Virtual second-order triangular and line elements constitute the integration domain, (b) details of the virtual mesh

$$I(s) = \sum_{A}^{\text{elems}} \sum_{p}^{\text{gpts}} \left\{ \left[\left(\sigma_{ij} \frac{\partial u_j^{\text{aux}}}{\partial x_1} + \sigma_{ij}^{\text{aux}} \frac{\partial u_j}{\partial x_1} - W_{\text{I}} \delta_{1i} \right) \frac{\partial q}{\partial x_i} \right] |\mathbf{J}| \right\}_p w_p - \sum_{\Gamma_- + \Gamma_+}^{\text{elems}} \sum_{p}^{\text{gpts}} \left[\left(\sigma_{2j} \frac{\partial u_j^{\text{aux}}}{\partial x_1} m_2 q \right) |\mathbf{J}| \right]_p w_p \quad (22)$$

where the summations over area A and contour $\Gamma_- + \Gamma_+$ include all the virtual triangular and line elements, respectively. The sum over p includes element integration points, 'gpts', of the virtual elements, 'elems', where the bracketed quantities $\{\}_p$ and $[]_p$ are evaluated and multiplied by the corresponding weight w_p. Repeated indices imply summation, and $|\mathbf{J}|$ denotes the determinant of the coordinate Jacobian matrix of the virtual triangular and bar elements.

The computation of area integrals in Eqs. (21) and (22) requires the computation of the stress, strain and displacement gradient tensors at the integration points of the virtual elements. These values have to be extracted from the FE solution over the tetrahedral element that contains the integration point of the virtual element. This requires the following steps: (i) The tetrahedral element containing the virtual integration point p is identified by using a search algorithm explained in Appendix C; (ii) The local coordinates of the point p inside the tetrahedral element are computed using the expressions in Appendix C. (iii) The stress, strain and displacement gradient

tensors of these integration points are directly obtained from the FE displacement solution over the tetrahedral element. All these quantities must be expressed in the local coordinate system $x_1x_2x_3$ located at point s on the crack front (see Fig. 5). The evaluation of line integrals also requires the computation of surface traction σ_{2j} and displacement gradient $\partial u_j/\partial x_1$ at the virtual integration point p on the crack surface. Computing these values also requires the following steps: (i) The triangular element that contains p is identified; (ii) The local coordinates of the point p in the triangular element are computed; (iii) σ_{2j} and $\partial u_j/\partial x_1$ at p are computed by interpolating the nodal tractions and displacement derivatives using the element shape functions (see Appendix C). It is also straightforward to compute the values for q-function and its derivative, and the auxiliary fields σ_{ij}^{aux}, and $\partial u_j^{\text{aux}}/\partial x_1$ at the virtual integration point p. This only requires substituting the position of p in the local coordinate system located at s into the q-function and analytical auxiliary fields expressions given in Appendix A. As q is a function of x_1 and x_2 only, the derivative with respect to x_3 vanishes ($\partial q/\partial x_3 = 0$). The procedure of computing J-integral and the SIFs is demonstrated in Algorithm (1).

All procedures employed in this work were implemented into the Geomechanics module (Paluszny and Matthäi, 2009; Paluszny and Zimmerman, 2011) of the Complex System Modeling Platform (CSMP++), an object-oriented finite element based API developed for the simulation of complex geological processes (Matthai et al., 2001). The system of equations resulting from the finite element method accumulation is solved using the Fraunhofer SAMG Solver (Stüben, 2001).

5. Numerical examples

In order to demonstrate the efficiency and accuracy of the proposed approach, the J-integral and stress intensity factors were computed for the following three crack configurations: (i) through-the-thickness crack in a large thin plate with lateral constraint (plane strain condition); (ii) penny-shaped crack embedded in an infinite solid; and (iii) elliptical crack embedded in an infinite solid, as shown in Fig. 6.

Algorithm 1 Evaluation of the pointwise J-integral and SIFs using the disk-shaped domain integral method

Generate a local coordinate system $x_1x_2x_3$ at the point s using the unit vectors b_1, b_2 and b_3.
Create a virtual disk-shaped integration domain using quadratic triangular and line elements.
for $e := 1 \rightarrow \mathrm{N_{tr}}$ **do**
  for $p := 1 \rightarrow \mathrm{N_P}$ **do**
    Find the tetrahedral element which contains the point p (Appendix C.1).
    Compute the local coordinates (ξ, η, ζ) of p in the tetrahedral element (Appendix C.1).
    Compute σ_{ij}, ϵ_{ij}, $\nabla \times u$ at p in the local coordinate system.
    Compute the auxiliary fields $\sigma_{ij}^{\mathrm{aux}}$, and $\partial u_j^{\mathrm{aux}}/\partial x_1$ at p (Appendix A) .
    Compute $\partial q/\partial x_i$ at p.
    Compute $|\mathbf{J}|$ at p using virtual triangular element coordinate matrix.
    Accumulate: $J(s) \leftarrow J(s) + \left[\left(\sigma_{ij}\dfrac{\partial u_j}{\partial x_1} - W\delta_{1i}\right)\dfrac{\partial q}{\partial x_i}\right]|\mathbf{J}|\, w_p$
    Accumulate: $I_{\mathrm{z}}(s) \leftarrow I_{\mathrm{z}}(s) + \left[\left(\sigma_{ij}\dfrac{\partial u_j^{\mathrm{aux}}}{\partial x_1} + \sigma_{ij}^{\mathrm{aux}}\dfrac{\partial u_j}{\partial x_1} - W_{\mathrm{I}}\delta_{1i}\right)\dfrac{\partial q}{\partial x_i}\right]|\mathbf{J}|\, w_p \quad \mathrm{z} = \mathrm{I}, \mathrm{II}, \mathrm{III}$
  end for
end for
for $e := 1 \rightarrow \mathrm{N_{li}}$ **do**
  for $p := 1 \rightarrow \mathrm{N_P}$ **do**
    Find the triangular surface element which contains the point p (Appendix C.2).
    Compute the local coordinates (ξ, η) of p in the triangular element (Appendix C.2).
    Compute the traction σ_{ij}, and $\nabla \times u$ at p in the local coordinate system.
    Compute the auxiliary field $\partial u_j^{\mathrm{aux}}/\partial x_1$ at p (Appendix A).
    Compute q at p.
    Compute $|\mathbf{J}|$ at p using virtual line element coordinate matrix.
    Accumulate: $J(s) \leftarrow J(s) - \left(\sigma_{2j}\dfrac{\partial u_j}{\partial x_1}m_2 q\right)|\mathbf{J}|\, w_p$
    Accumulate: $I_{\mathrm{z}}(s) \leftarrow I_{\mathrm{z}}(s) - \left(\sigma_{2j}\dfrac{\partial u_j^{\mathrm{aux}}}{\partial x_1}m_2 q\right)|\mathbf{J}|\, w_p \quad \mathrm{z} = \mathrm{I}, \mathrm{II}, \mathrm{III}$
  end for
end for
Compute SIFs from Eq. (12)

▷ $\mathrm{N_{tr}}$, $\mathrm{N_{li}}$, and $\mathrm{N_P}$ are the numbers of virtual triangular elements, virtual line elements, and the element's integration points, respectively. ▷ $I_{\mathrm{z}}(s)$ is computed using the auxiliary fields of crack deformation mode z.

5.1. Experimental setup

All the crack bodies are subjected to a uniform uniaxial tension in the X_2 direction over the top and bottom surfaces. The cracks lie in the plane $X_2 = X_1 \cot\beta$ which generates the angle of β with the direction of applied load. A horizontal crack configuration ($\beta = 90°$) produces pure mode I crack deformation, while the inclined one ($0° < \beta < 90°$) provokes a mixed-mode condition. In these configurations, a denotes half of the crack length for the through crack, crack radius for the penny-shaped crack, and semi-major axis for the elliptical crack. The semi-minor axis b of the elliptical crack is perpendicular to the X_1X_2 plane. The crack length to body width ratio of $a/w = 0.1$ was used for all the cracked bodies. The crack length to the plate thickness of $a/t = 1$ was considered for the through-the-thickness crack. As the fracture parameters of these crack configurations are independent of the value of Young's modulus, an arbitrary value of $E = 1$ was used in all models. The choice of Poisson's ratio is not arbitrary, as the mode II and III SIFs of embedded cracks depend strongly on the value of this material property (see analytical solutions in Appendix D). In this work, a Poisson's ratio of $\nu = 0.3$ was used for all simulations.

5.1.1. Boundary conditions

Due to the symmetry in geometry and loading conditions, only one-eighth ($X_1 > 0, X_2 > 0, X_3 < 0$) and one-half ($X_3 < 0$) of the cracked bodies were modeled for pure mode I ($\beta = 90°$) and mixed-mode ($\beta = 45°$) conditions, respectively. The following boundary conditions were applied for mode I models: $u_1 = 0$ over the plane $X_1 = 0$, $u_2 = 0$ over the plane $X_2 = 0$ except over the crack surface, $u_3 = 0$ over the plane $X_3 = 0$, and $\sigma = 1$ over the plane $X_2 = w$. The applied boundary conditions for the mixed-mode models are also as follows: $u_1 = 0$ at the point $X_1 = X_2 = -w, X_3 = 0$, $u_2 = 0$ over the plane $X_2 = -w$, $u_3 = 0$ over the plane $X_3 = 0$, and $\sigma = 1$ over the plane $X_2 = w$. For the through-the-thickness crack, the following additional boundary condition was also applied, to ensure zero lateral displacement: $u_3 = 0$ over the plane $X_3 = -t$. This boundary condition imposes a plane strain condition over the cracked plate, where the pointwise SIFs at any point on the crack front follows the solution of the equivalent 2D problem of an

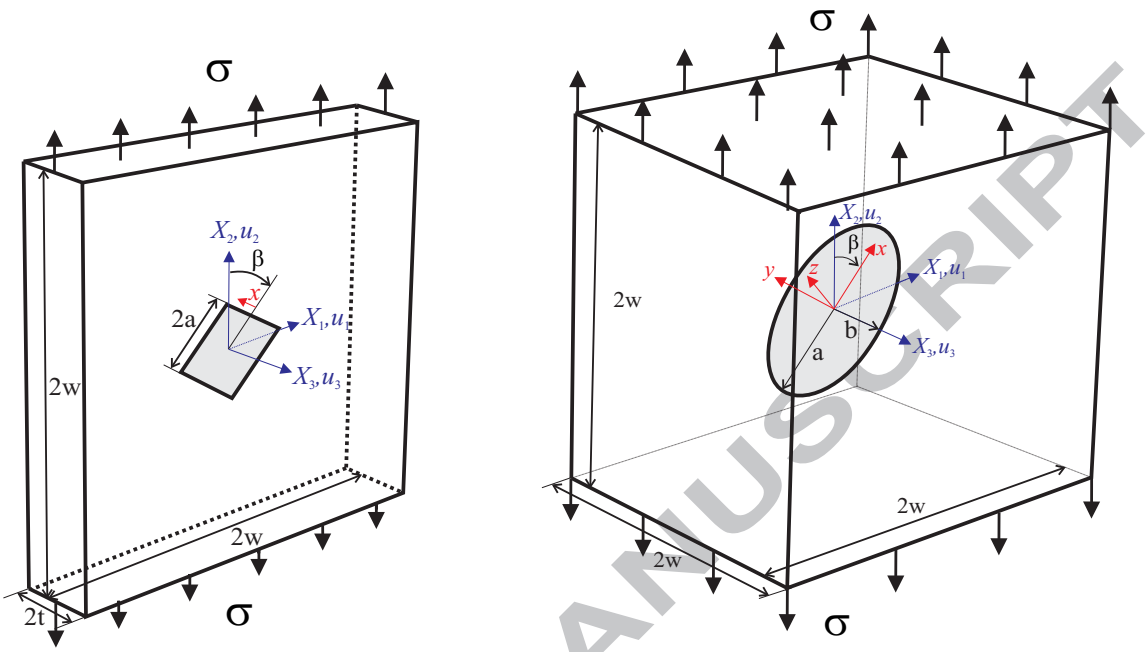

Figure 6: Schematics of (a) Through-the-thickness crack in a large thin plate under uniaxial tension; (b) Penny-shaped/elliptical crack embedded in an infinite solid under uniaxial tension.

inclined central crack in a large plane. This solution gives the SIFs as follows: $K_{\mathrm{I}} = \sigma\sqrt{\pi a}\sin^2\beta$, $K_{\mathrm{II}} = \sigma\sqrt{\pi a}\sin\beta\cos\beta$, and $K_{\mathrm{III}} = 0$. These formulas along with the analytical solutions for the SIFs of embedded inclined penny-shaped and elliptical cracks in infinite solids given in Appendix D will be used to validate the numerical results.

5.1.2. Mesh

An octree-based mesh generation software was employed to generate arbitrary meshes for all specimens, using 10-noded isoparametric tetrahedal elements. For the elements attached to the crack front, the nodes near the front are moved from the mid-side point to the quarter-point position to produce inverse square root singular fields near the front. The curved crack fronts impose one curved edge for the tetrahedral elements sharing an edge with the crack front. When using quarter-point elements, the Jacobian determinant over small volume near the curved edges becomes negative. To avoid this, the curve edges were straightened by moving the mid-side nodes

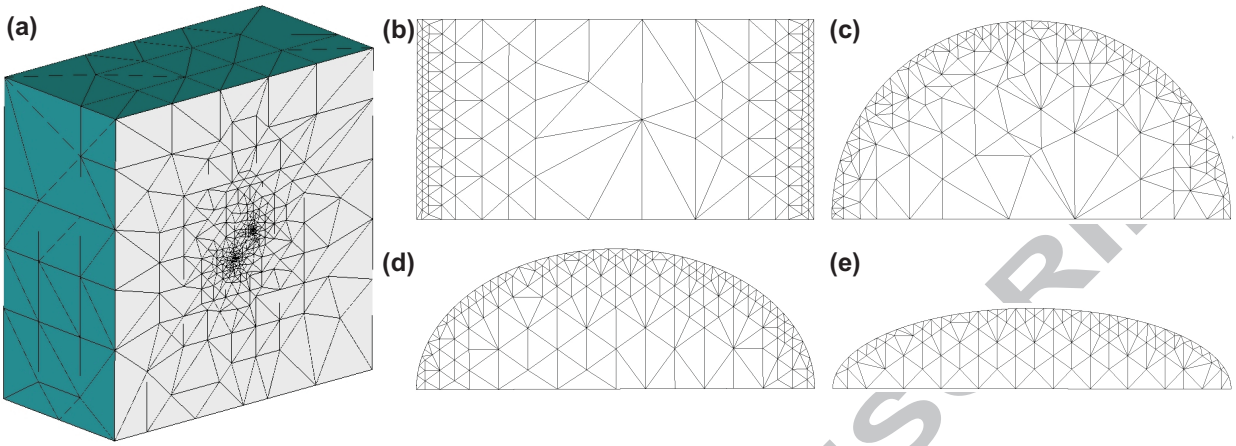

Figure 7: (a) Finite element mesh discretizing one-half of an embedded penny-shaped crack; Details of mesh in crack-front region for (b) through-the thickness, (c) penny-shaped, (d) elliptical ($b/a = 0.7$), (e) elliptical ($b/a = 0.4$) cracks. For all cases $L_n \approx a/20$.

of the curved segments. The refinement of mesh near the crack front was controlled by assigning the number of segments along the crack front. Assume that the crack front of length L_f is discretized by N_f segments. A parameter called the nominal length (size) of the elements in the crack front region can be defined as $L_n = L_f/N_f$. The nominal element length L_n represents the approximate length of the elements' sides near the crack front, and therefore gives an approximate for the average size of the tetrahedral elements in the crack front region. In all models, the degree of mesh refinement in the crack front region was controlled by keeping the nominal crack front element size about one twentieth of the crack length ($L_n \approx a/20$). As estimations suggest that the size of the singular dominant zone depends mainly on the crack length, ranging between $a/10$ and $a/50$ (Kuna, 2013), keeping $L_n \approx a/20$ ensures that the quarter-point elements at the crack front predominantly remain in the singular dominant zone where the fields have the inverse square root singularity. Four-point, three-point, and two-point Gaussian quadrature rules were employed for the numerical integration over tetrahedral, triangular, and bar elements, respectively. Figure (6) shows the finite element mesh of the penny-shaped crack problem together with the local mesh refinements near the crack front in different crack configurations.

5.1.3. Domain size and virtual mesh

For all crack configurations, the mesh-dependent domain radius of $R_d = L_n$ has been used to generate the virtual domains and compute the fracture parameters. Domains were built at the locations of both corner and mid-side nodes of the segments along the crack front. The refinement of the virtual mesh is controlled by the number of domain elements in the radial direction k as shown in Fig. 5. A similar virtual mesh structure as the one shown in Fig. 5, with four elements in radial direction ($k = 4$), was used to compute the fracture parameters. This choice yields 112 quadratic triangular elements, containing 112×3 integration points, together with 8 quadratic line elements, containing 8×2 integration points. The reasons for these choices are explained in Sections 6.1 and 6.2.

5.1.4. The scalar function q

In order to compute the fracture parameters, a smooth function q must be defined over the domain (disk) area. All the numerical results in this research are determined by using $q = 1 - r/R_d$, where $r = \sqrt{x_1^2 + x_2^2}$ is the distance from disk center and R_d is the domain radius (see Fig. 5). The derivatives of this function ($\partial q/\partial x_1 = -x_1/rR_d$ and $\partial q/\partial x_2 = -x_2/rR_d$) are directly evaluated at the integration points of the virtual triangular elements. Section 6.3 explains how numerical results are influenced by changing this function.

5.2. Numerical results

After the computation of the pointwise SIFs along the crack fronts, the average numerical error of SIF computation for individual modes e_{i} ($\mathrm{i} = \mathrm{I}, \mathrm{II}, \mathrm{III}$) and average total error e_{t} were evaluated by using Eq. (23). In these expressions, K_{i}^A and K_{i}^N are the pointwise analytical and numerical mode i SIFs, respectively, and L_f is the crack front length. Wherever closed form integration was not available, a trapezoidal rule has been employed to evaluate the integrals numerically.

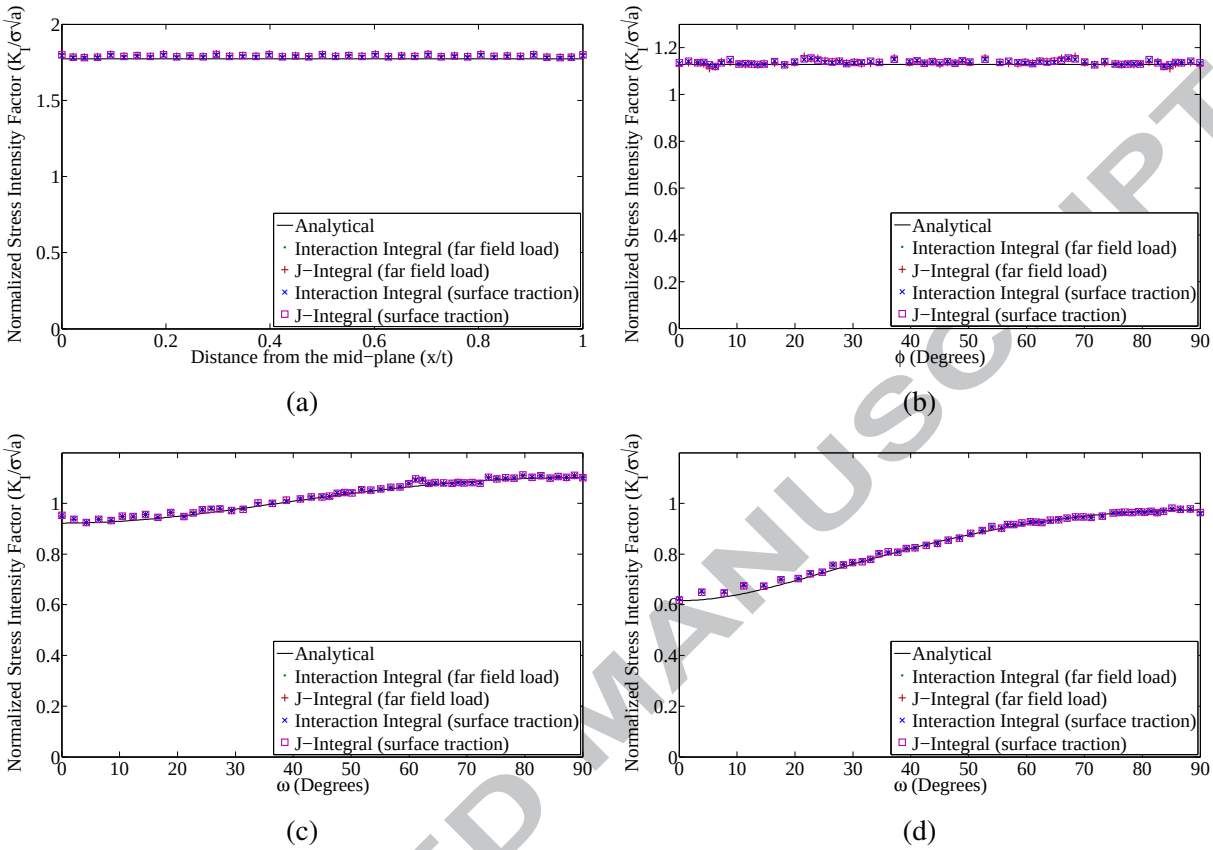

Figure 8: The variation of normalized mode I ($\beta = 90°$) analytical and numerical SIFs along the fronts of (a) through-the-thickness, (b) penny-shaped, (c) elliptical ($b/a = 0.7$), (d) elliptical ($b/a = 0.4$) cracks using J- and interaction integrals. The mode I average error is as follows: (a) $e_{\mathrm{I}} = 0.011$, (b) $e_{\mathrm{I}} = 0.008$, (c) $e_{\mathrm{I}} = 0.008$, (d) $e_{\mathrm{I}} = 0.008$.

$$e_{\mathrm{i}} = \frac{\int_{L_f} |K_{\mathrm{i}}^A - K_{\mathrm{i}}^N| \mathrm{d}l}{\int_{L_f} |K_{\mathrm{i}}^A| \mathrm{d}l} \quad \mathrm{i} = \mathrm{I}, \mathrm{II}, \mathrm{III} \qquad e_{\mathrm{t}} = \frac{\sum_{\mathrm{i=I}}^{\mathrm{III}} \int_{L_f} |K_{\mathrm{i}}^A - K_{\mathrm{i}}^N| \mathrm{d}l}{\sum_{\mathrm{i=I}}^{\mathrm{III}} \int_{L_f} |K_{\mathrm{i}}^A| \mathrm{d}l} \tag{23}$$

5.2.1. Mode I loading condition

Fig. 8 shows the variation of the pointwise mode I stress intensity factor along the crack front of different crack configurations when $\beta = 90°$. Analytical solutions for a 2D plane strain central crack problem, and 3D penny-shaped and elliptical cracks embedded in infinite solids (Appendix D) are also plotted. Here, ϕ and ω are the polar angle of the circle, and the parametric angle

of the ellipse, respectively. The numerical K_{I} values have been computed by the evaluation of J- and interaction integrals in Eqs. (21) and (22), and their substitution into Eqs. (9) and (12) for the following loading conditions: (i) the specimens are subjected to original far field load σ as shown in Fig. 6; (ii) instead of applying the load at the far field, σ was applied over the fracture surface. These loading conditions are equivalent according to the superposition principle, generating identical SIFs. The average error e_{I} for any of these four sets of results is about 1%. Highly accurate values in the case of surface tractions demonstrate the efficiency of line elements for accurate numerical computation of surface traction integrals.

5.2.2. Mixed-mode loading condition

Fig. 9 shows the variation of pointwise mixed-mode SIFs along the crack front of four different crack configurations when $\beta = 45°$. The average total error e_{t} for all the cases is about 1%. These results are obtained from a relatively coarse mesh (see Fig. 7), and a finer mesh will result in the computation of even more accurate SIFs. These results demonstrate the efficiency of the disk-shaped domains to accurately compute the interaction integral from arbitrary meshes. Section 6 discusses the effects of actual and virtual mesh refinements as well as domain radius on these results.

5.2.3. Evaluation of SIFs near the meeting point of crack front and free surface

Consider the through-the-thickness crack problem, when no lateral constraint is applied to the plate, leaving the lateral surfaces to be traction free. The main characteristics of the behavior in this cracked body are: (i) At the intersection of the crack front and free surface a corner singularity occurs, where the order of the singularity, which depends on Poisson's ratio as well as on the loading conditions, is different from the crack singularity (Benthem, 1977; Bažant and Estenssoro, 1979). As a result, at the exact corner point the definition of crack stress intensity factor loses its meaning, since an inverse square root singular field no longer exists (Nakamura and Parks, 1988, 1989). (ii) Modes II and III become coupled, meaning that applying primary shear or anti-plane

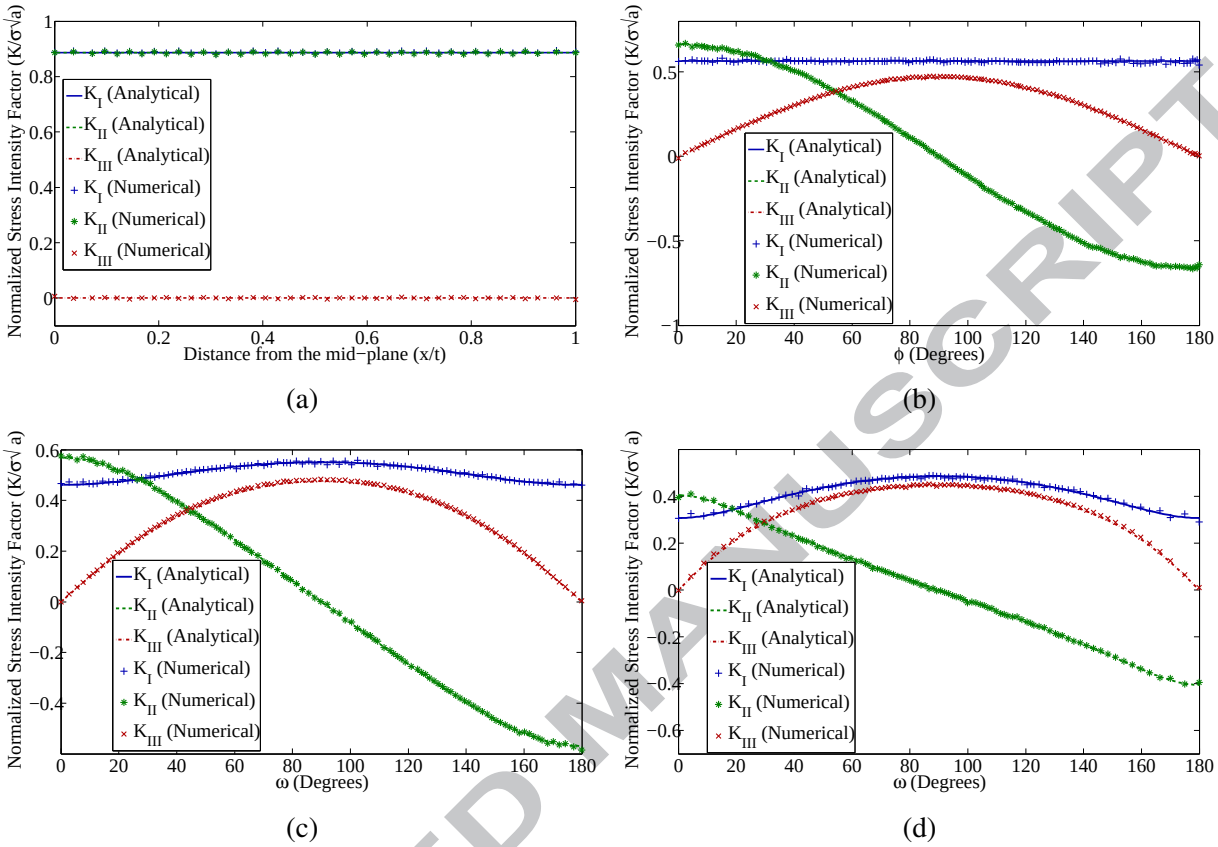

Figure 9: The variation of normalized mixed-mode ($\beta = 45°$) analytical and numerical SIFs along the fronts of (a) through-the-thickness, (b) penny-shaped, (c) elliptical ($b/a = 0.7$), (d) elliptical ($b/a = 0.4$) cracks. The average total SIF computation error is as follows: (a) $e_t = 0.005$, (b) $e_t = 0.011$, (c) $e_t = 0.012$, (d) $e_t = 0.013$.

loading on the plate also generates a coupled mode III, or mode II crack deformation, respectively (Bažant and Estenssoro, 1979; Nakamura and Parks, 1988, 1989; Kotousov et al., 2013). This coupling occurs due to the Poisson's ratio effect or the redistribution of stresses near the free surfaces (Kotousov et al., 2010, 2013; Pook et al., 2014). For example, when a primary mode II crack deformation ($K_{II} > 0$) is applied to the cracked plate, a coupled mode III deformation also occurs due to the Poisson's effect, as the plate above the crack plane is expanded along thickness direction, while the region below the crack plane is contracted. It has been shown that the intensities of the coupled modes can be as strong as those of primary modes (Kotousov et al., 2013). Because of these two characteristics, the strong 3D effects influences the stress fields near the crack front,

and a classical two-dimensional (plane) elasticity solution is no longer able to reproduce the stress intensities along the crack front.

Now assume that a primary mixed-mode I/II load is applied on a through-the-thickness crack with traction free surfaces. A few characteristics of the SIF variation along the crack front must be noted: (i) As explained earlier, although the cracked plate is primarily subjected to a mixed-mode I/II loading condition, a couple mode III crack deformation is also created due to the Poisson's effects. (ii) Under symmetric loading, the corner singularity is weaker than the crack singularity, and therefore the local K_{I} must approach zero at the free surface (Nakamura and Parks, 1988; Benthem, 1977; Bažant and Estenssoro, 1979; Benthem, 1980; He et al., 2015). This does not mean that the stress is finite at the corner point, but it demonstrates that K_{I} cannot be used to characterize the fields at the corner point. (iii) On the other hand, for the antisymmetric loading condition, the corner singularity is stronger than a crack singularity, and therefore the local K_{II} approaches infinity at the free surfaces (Nakamura and Parks, 1989; Benthem, 1977; Bažant and Estenssoro, 1979; Benthem, 1980; He et al., 2015). (iv) The coupled mode III deformation behaves differently compared to K_{I} and K_{II} since K_{III} must be zero at mid-plane and free surfaces due to the symmetry and traction free boundary conditions, respectively. In fact, K_{III} is zero at the mid-plane, reaches its maximum near the free surface, and drops back to zero at the corner point (Harding et al., 2010; Kotousov et al., 2010, 2013). This behavior is not observed in the results of Nakamura and Parks (1989) as the coupled mode III SIF, which were computed using volumetric domain integral approach, appears to approach infinity at the free surface. Such behavior is inconsistent with the free boundary conditions and zero anti-plane shear stress at the free surfaces. This inconsistency has been noticed by Harding et al. (2010); Kotousov et al. (2010), as the K_{III} values they computed using the stress extrapolation method deviates from the ones obtained by Nakamura and Parks (1989) for the points very close to the corner point. The reason for this inconsistency has not been investigated previously.

The proposed method is now used to compute the SIFs of a plate with traction free lateral

surfaces containing an inclined through-the-thickness crack with $\beta = 45°$. A very fine mesh ($L_n = a/400$) was generated, and the SIFs at nodes along the crack front were computed using the disk-shaped domains of radius $R_d = 2L_n$. Fig. 10a shows the variation of SIFs against the normalized distance from the mid-plane x/t. The specimen was also modeled and analyzed with Abaqus, where a structured mesh by collapsed quarter-point hexahedral elements with an equivalent crack front region mesh density was used. The SIFs were computed using an equivalent cylinder radius of $R_d = 2L_n$ in the contour integral module of this commercial FE package. The module uses the volumetric cylindrical domains explained in Section 2 to compute the SIFs (Abaqus, 2012). These results are plotted against the normalized distance from the mid-plane in Fig. 10a. A comparison of the two methods shows that the results are in very close agreement, except very near the corner point $x/t = 1$. The results from both methods demonstrate that K_{I} and K_{II} approach zero and infinity, respectively. However, the coupled K_{III} results from the cylindrical domains tend to infinity, similar to the trend reported in Nakamura and Parks (1989), while those from disk-shaped domains seem to approach zero, which is in consistency with the trend reported by Harding et al. (2010); Kotousov et al. (2010, 2013). Let us now use Eq. (19) instead of Eq. (20) to evaluate the integrals for the disk-shaped domains. Eq. (19) contains one more term, the second term, where in-plane and anti-plane crack tip fields are coupled in the process of SIF computation. This term vanishes in Eq. (20) by employing the superposition principle, as discussed in Section 3. The following steps were taken to compute this term: (i) the integral associated with this term was computed at the points along the crack fronts; (ii) at each point a polynomial equation was fitted locally to the integral values using the least square scheme; (3) the derivative of the polynomial was computed at the point. Fig. 10b shows the variation of SIFs computed by Eq. (19) against the normalized distance from the mid-plane. As is seen, the results of the disk-shaped domains are now consistent with cylindrical domains, providing questionable trend for K_{III} near the corner point.

Consider the integral term developed by substituting $i = 3$ into Eq. (6). This integral term is

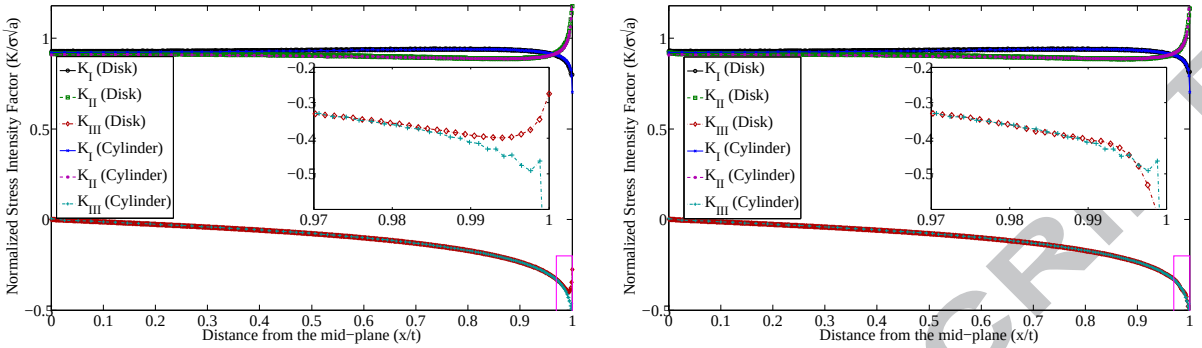

Figure 10: The variation of normalized numerical SIFs along the through-the-thickness crack front when the lateral surfaces are traction free ($\beta = 45°$). For both plots the cylinder results are computed from cylindrical domains using Abaqus contour integral module. Eqs. (20) and (19) are used respectively to compute disk results for (a) and (b).

evaluated over the tubular domain shown in Fig. 2. Also consider the function q over the Volume V as $q = q'(x_1, x_2)q''(x_3)$ where $q'(x_1, x_2)$ describes the variation of q over a disk-shaped area A, and $q''(x_3)$ describes the variation of q along the small crack front segment L_c (see Fig. 3). If the crack fields vary slightly along L_c, the integral $\int_A \sigma_{3j}\partial u_j/\partial x_1 q'(x_1, x_2)$ can be assumed to behave linearly along L_c. Using integration by parts, therefore, the term $i = 3$ in Eq. (6) can be expressed in the form of an area integral as

$$\frac{\int_V \sigma_{3j}\dfrac{\partial u_j}{\partial x_1}\dfrac{\partial q}{\partial x_3}\mathrm{d}V}{\int_{L_c} q(x_3)\mathrm{d}x_3} = -\frac{\partial}{\partial x_3}\int_A \sigma_{3j}\frac{\partial u_j}{\partial x_1}\, q'(x_1, x_2)\mathrm{d}A \tag{24}$$

where A is the disk-shaped area developed when an orthogonal plane to the crack front intersects the tubular region V at the mid-point of L_c (see Fig. 3). A similar equivalent area integral can be found for the term developed when $i = 3$ is substituted in the first term of Eq. (13). These relations indicate that the volumetric versions of domain integrals in Eq. (6) and (13) approximately evaluate the second terms of the disk-shaped domain integral formulas in Eqs. (16) and (19). As discussed in Sections 3.1 and 3.2 these terms couple the fields from in-plane and anti-plane loads.

It was then shown that, by applying the superposition principle, these terms can be eliminated, and Eqs. (17) and (20) were suggested for the disk-shaped domain integral formulations. The inaccurate trend of K_{III} near the corner point when using volumetric domain integrals can be attributed to the presence of these terms in their formulation. Strong variation of modes I/II fields occurs near the corner point, and the gradients of these fields with respect to x_3 are high enough to influence K_{III} significantly via the coupling term developed by substituting $i = 3$ in Eq. (13), or the second term in Eq. (19). Such an influence is not allowed in the disk-shaped domain formulation proposed in this research i.e. Eq. (20); therefore this formulation can reproduce a more accurate variation of SIFs near the corner point. It must be noted that the values of SIFs in Fig. 10a may vary slightly by using a finer mesh, but the trend remains the same. It is generally advised that a more refined mesh is used to compute more accurate values of the SIFs near the corner point.

6. Discussion

Three parameters mainly influence the computation of the fracture parameters using the proposed method: mesh refinement at crack front region, virtual mesh refinement of the disk, and domain (disk) size. The domains must remain in the singular dominant region, where a plane strain condition prevails. Thus, one should avoid using large domains compared to the crack sizes. However, a very small domain may capture only the fields available from the FE solution, which are not accurate enough to represent crack tip fields. Therefore, for every mesh resolution, there will be an optimum domain size at which the computed fracture parameters are the most accurate. As the degree of the accuracy of the fields near the crack depends on the type and refinement of the elements in that region, it is expected that the optimum domain size depends mainly on the type and size of the elements in the crack front region. To clarify the dependency of the proposed domain integral approach on these three parameters, an extensive parametric study is carried out in this Section. The SIFs of the crack configurations described in the previous section were computed while changing these three parameters, and the formulas in Eq. (23) were used to evaluate

the average of total SIF computation error.

6.1. Refinement of virtual mesh

Consider the virtual mesh structure shown in Fig. 5 with k and $4 \times k$ grids in the radial and circumferential directions, respectively. In this mesh structure, k controls the virtual mesh refinement by generating $4 \times k(2 \times k - 1)$ virtual triangular elements and $2 \times k$ line elements. The crack front of length L_f is discretized by N_f segments. The nominal size of the elements in the crack front region is defined as $L_n = L_f/N_f$, which quantifies the refinement of the actual mesh in the crack front region. Figure (11) shows the variation of average total SIF error e_{t} for different actual mesh refinements, a/L_n, versus the number of virtual elements in radial direction, k, used to compute the SIFs of the penny-shaped crack for two domain radiuses $R_d = a/10$ and $R_d = a/20$. In both virtual and actual meshes, quarter-point elements have been used at the immediate crack front region. These graphs demonstrate the following: (i) The virtual elements are very efficient in capturing the crack fields, as accurate values can be computed for the SIFs even when very coarse virtual elements are employed ($k = 1$), and using more refined mesh does not significantly change the SIFs. This is mainly because the quarter-point virtual elements are very accurate and efficient in numerical integration of singular fields (see Appendix B). (ii) The SIF computation error drops slightly by increasing k to 4, remaining steady for greater values of k. A similar behavior was also observed in other crack configurations and other choices of the domain radius. This suggests that the choice of $k = 4$ generates a sufficiently refined virtual mesh that is able to capture all the crack tip field variations that a very refined actual mesh can reproduce. This finding allows the virtual mesh density to be chosen independent of the actual mesh refinement, and of the domain size. It is recommended that $k = 3, 4$ be used for the fast and efficient computation of SIFs, and $k = 5, 6$ for a more robust SIFs computation.

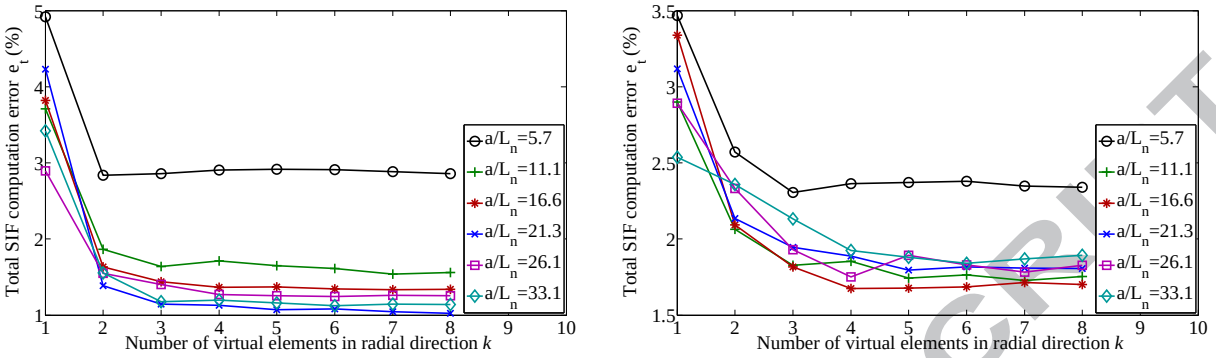

Figure 11: The variation of the total SIF computation error e_t of the penny-shaped crack under mixed-mode loading condition ($\beta = 45°$) versus the number of the virtual elements in the radial direction k in different mesh refinements: (a) $R_d = a/20$, (b) $R_d = a/10$.

6.2. Disk (domain) radius

An optimum size is expected to exist, which depends on the local actual mesh refinement in the front region. A very large domain compared to the crack size leads to the violation of the basic assumption of having a plane strain condition within the domain. The domain radius, therefore, must be chosen to be as small as possible. The size of the singular dominant zone can be considered as an upper bound for the domain radius. This requires the domain radius to be smaller than the size of the singular dominant zone which mainly depends on the characteristic crack length, ranging between a/10 and a/50 (Kuna, 2013). However, very small domains might also introduce high errors since the closer to the crack front, the higher the error of FE fields (Paluszny and Zimmerman, 2011). In addition, crack tip fields are obtained from the FE solution, where the equilibrium equations are satisfied on the average within the element. Therefore, domains significantly smaller than crack front elements may not capture the crack tip fields properly. Given these facts, the appropriate domain size is found to be a balance between the satisfaction of prior assumption of plain strain fields and the accuracy of FE fields in the domain. In an arbitrary mesh around the crack front, the size of the elements may vary significantly, and an approximate (nominal) value should be used to represent the average size of the elements. The nominal element

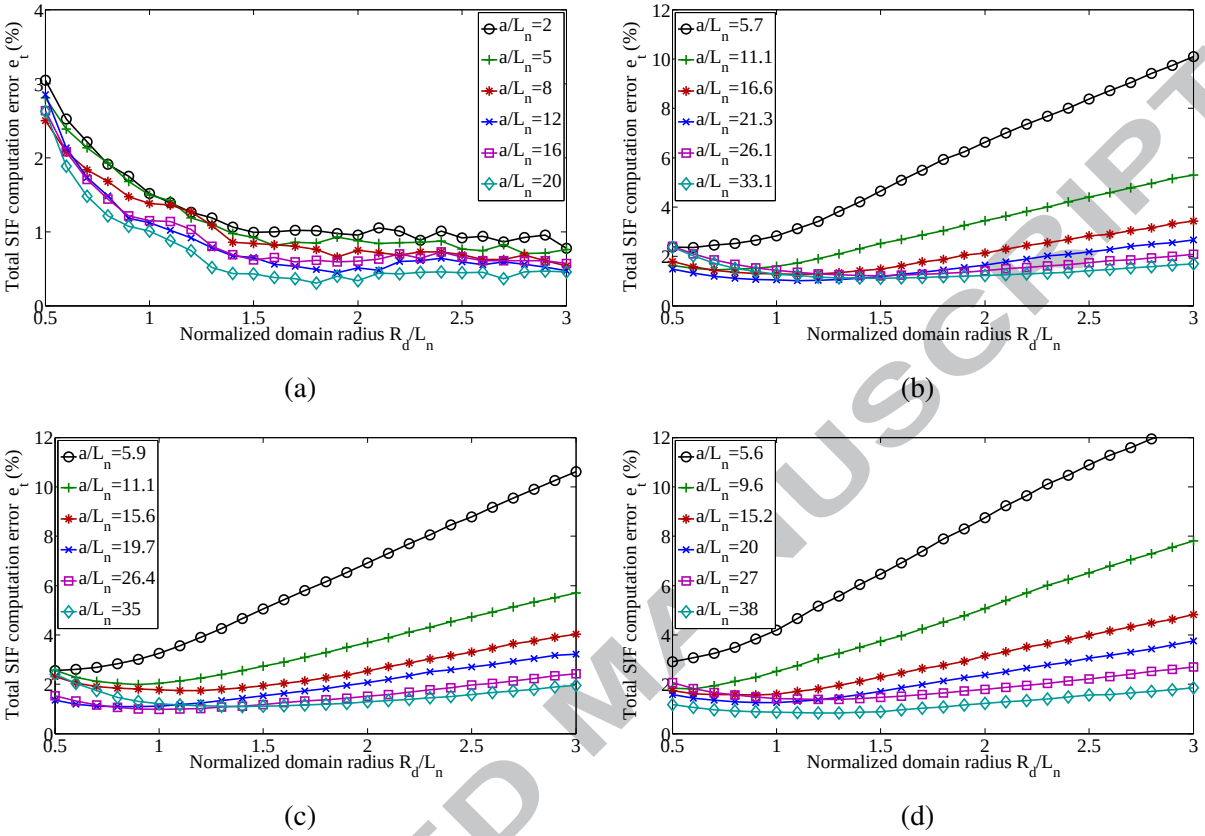

Figure 12: The variation of the total numerical error e_t against the normalized domain radius R_d/L_n for (a) through-the-thickness, (b) penny-shaped, (c) elliptical ($b/a = 0.7$), (d) elliptical ($b/a = 0.4$) cracks in different mesh refinements when using quarter-point tetrahedral elements.

size $L_n = L_f/N_f$ is defined, where L_f and N_f are the length of the crack front and number of segments used to discretize it, respectively. To investigate the idea of an optimum domain size, an extensive parametric study was carried out to relate the SIF computation error to the domain radius in different mesh refinements. The SIFs of the different crack configurations were computed for different domain radiuses in different actual mesh densities, while the virtual mesh density was kept constant by $k = 6$. This fine virtual mesh ensures that all the field variation in different actual mesh refinements and domain radiuses are captured. Quarter-point elements were employed in the crack front region in both actual and virtual meshes.

Figure (12) shows the variation of the average total SIF computation error versus the nor-

malized domain radius R_d/L_n for different actual mesh refinements expanding from very coarse meshes $a/L_n \approx 5$ to very fine meshes $a/L_n \approx 35$. The main features of the results in these graphs are as follows: (i) For the through crack, the error e_t drops slightly from $R_d = 0.5L_n$ to $R_d = 1.5L_n$, at which point it stabilizes. As the whole plate is under plane strain conditions, 2D plane strain crack tip fields are developed ahead of the crack front, and therefore the fracture parameters can be computed very accurately, even when using very large domains. This is not the case for the other crack configurations, where the plane strain condition prevails only close to the crack front. (ii) For the embedded penny-shaped and elliptical cracks, except very coarse meshes, e_t slightly drops by increasing the domain radius, reaching its minimum between $R_d = L_n$ and $R_d = 1.5L_n$, and then increases gradually for larger domain sizes. The decreasing trend in the beginning is explained by the fact that increasing the domain size allows the capture of more representative crack tip fields, and also, the overall influence of local numerical errors decreases as integration is performed over a larger domain. The growth trend is because a larger domain is more likely to include the areas at which the plane strain condition no longer prevails. The plots clearly show that there exists an optimum domain radius at which the error hits its minimum. This behavior is not observed for the very coarse mesh, as the domains are already very large compared to the crack size, and the minimum error is more likely to occur at $R_d \approx 0.5L_n$. According to these results, it can be concluded that there exists a mesh dependent optimum domain radius in the range of $0.5L_n \leq R_d \leq 1.5L_n$, where the SIF computation error is minimum. The optimum radius approaches $R_d = 0.5L_n$ and $R_d = 1.5L_n$ for coarse and fine meshes, respectively, and a domain radius of $R_d = L_n$ is the best choice that works for both fine and coarse meshes.

Figure (13) presents the variation of the total SIF computation error versus the normalized domain radius R_d/L_n, when standard tetrahedral elements are employed at the crack front region instead of quarter-point ones. Equivalently, instead of quarter-point triangular elements, standard quadratic triangular elements are used at the first row in the virtual mesh. The main features of the results in these plots are as follows: (i) The SIF computation error is significantly higher

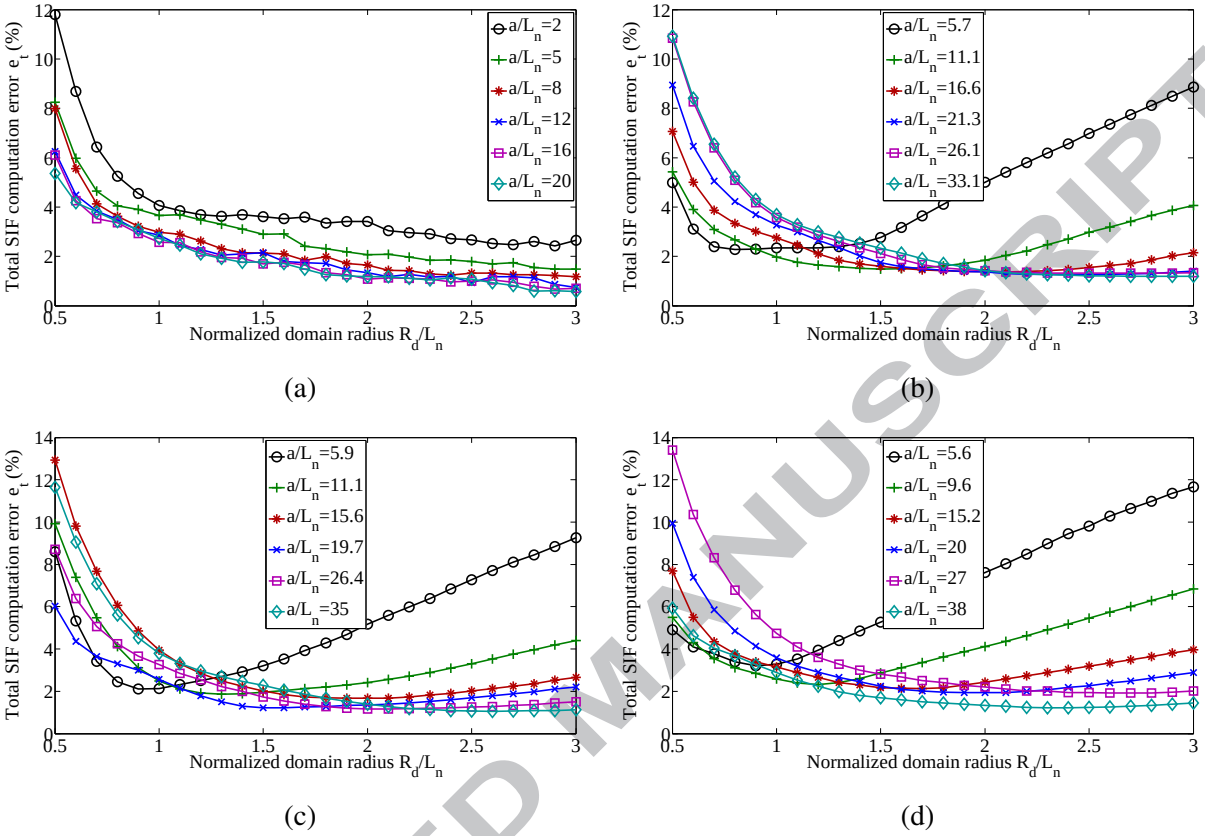

Figure 13: The variation of the total numerical error e_t against the normalized domain radius R_d/L_n for (a) through-the-thickness, (b) penny-shaped, (c) elliptical ($b/a = 0.7$), (d) elliptical ($b/a = 0.4$) cracks in different mesh refinements and in the absence of quarter-point tetrahedral elements.

in these plots compared to the ones in Fig. 12, especially at small domain sizes. The errors in these plots are approximately two to three times larger than the errors in Fig. 12. This highlights the efficiency of the quarter-point elements in improving the numerical solution of the crack tip fields. (ii) Similar trends are observed in these plots to those shown in Fig. 12. One important difference is that the errors for the small domains are significantly higher than those shown in Fig. 12. This indicates that when standard tetrahedral elements are used, larger domains should be preferred to compute accurate SIF values. (iii) The plots clearly demonstrate the existence of an optimum mesh-dependent domain radius at which the SIF computation error hits its minimum. This optimum domain radius is generally in the range of $L_n \leq R_d \leq 3L_n$ approaching $R_d = L_n$

and $R_d = 3L_n$ for very coarse and fine meshes, respectively. A domain radius of $R_d = 1.5L_n$ is suggested as the best choice, that works for both fine and coarse meshes.

6.3. The choice of the q-function

As was explained in Sections 2 and 3, an arbitrary continuously differentiable, the class C^1, scalar function q has to be defined over the domain. In order to assess the influence of different q functions, the SIFs of the penny-shaped crack were computed using the q function $q = 1 - (r/R_d)^n$ with the following four different powers: $n = 0.5, 1, 1.5, 2$. The model specifications such as actual mesh refinement, virtual mesh refinement and domain radius are the same as the ones given in Section 5.1. The average total SIF error e_t is as follows: $e_t = 5\%$ for $n = 0.5$; $e_t = 1.1\%$ for $n = 1, 1.5$; and $e_t = 1.2\%$ for $n = 2$. The reason for the high numerical error in the case $n = 0.5$ seems to be due to the fact that the derivatives of q function become singular at the disk center. This results in a less accurate numerical integration over the domain. Additionally, due to the singularity at the disk center, the sampling points near the disk center contributes to the entire integral much more than do the points near the disk boundaries. As the numerical error near the crack front is larger, it is expected that such a weighing process will lead to a larger numerical error in the computation of the SIFs. The accuracy of the results for the other three cases $n = 1, 1.5, 2$ seems to be about the same. However, an increase in n results in a higher average error, e_t. In particular, the individual mode III error e_{III} grows significantly for $n > 2$. The reason for such behavior is that increasing n makes the contribution of the sampling point near the boundaries more significant than the points near the crack front. This induces another source of error due to the fact that only near the crack front a plane strain state prevails, and far from the crack front a 3D stress state is more likely to exist. To summarize, it is concluded that q function should be chosen in a way that all sampling points contribute evenly to the entire integral. Therefore, the function $q = 1 - (r/R_d)$ is a suitable choice since (i) the linear variation of its derivatives can be captured well in the numerical integration, and (ii) the sampling points all over the domain contribute evenly to the entire integral.

6.4. The choice of crack front points

In this paper the pointwise SIFs are reported at the position of both corner and mid-side nodes of the crack front segments. However, disk-shaped domains can be constructed at any point along the crack front, and not necessarily at the position of crack front nodes. To assess the influence of the choice of points on the numerical results, the pointwise SIFs of the penny-shaped crack, whose specifications are explained in Section 5.1, were computed for the following sets of points separately: (i) positions of corner nodes of crack front segments; (ii) positions of mid-side nodes of crack front nodes; (iii) positions of midpoints between corner and mid-side nodes of the crack front segments. The average SIF error remains about 1% for all cases. This indicates the choice of the points on the crack front does not influence the accuracy of the SIFs, and therefore the pointwise SIFs can be computed accurately at any point along the crack front.

6.5. Potential extension of the method

The main focus of the present research is the computation of SIFs as the dominant influential parameters near the crack front. Numerical and experimental results have recently demonstrated that higher order terms of the crack tip asymptotic field, in particular T-stress, can also significantly influence the stress distribution near the crack tip, and consequently the onset of fracture growth (Smith et al., 2001; Ayatollahi et al., 2006; Berto and Lazzarin, 2010). Therefore, accurate computation of higher order parameters is also of great importance in analyzing the growth of cracked bodies. The method presented here can be readily extended to compute the T-stress in 3D cracked bodies based on the original works by Kfouri (1986) and Toshio and Parks (1992) that describe contour and domain integral formulations for evaluating the T-stress. The proposed methodology is also applicable to determine the notch stress intensity factors of sharp isotropic and bi-material V-notches, which makes it possible to efficiently use unstructured meshes to analyze V-notched structures.

7. Conclusions

A novel, efficient and accurate domain integral approach has been proposed for computing pointwise J-integral and stress intensity factors of 3D crack configurations from unstructured meshes. This method is based on the evaluation of domain integrals over disk-shaped domains, and has the following advantages over volumetric domain approaches that are based on tubular domains:

1. It can be directly applied to arbitrary tetrahedral meshes.
2. It requires less computational cost, as it performs integration over a disk rather than a tube.
3. It directly applies the original definition of the pointwise J- and interaction integrals.
4. Integration is performed over a disk perpendicular to the crack front, which is easy to generate and low in cost, and expressing the field in curvilinear coordinates is no longer required for curved cracks.
5. As 2D plane strain auxiliary fields satisfy compatibility and equilibrium equations over a disk, the term containing the higher order gradients of the auxiliary fields vanishes in this new formulation.
6. The in-plane and anti-plane fields are separated, and cannot influence each other in the computation of fracture parameters.

This method utilizes disk-shaped domains discretized with virtual triangular elements, which can be readily implemented in any FE code. The results of this method have been validated for a number of crack configurations in mode I and mixed-mode loading conditions, where the SIF computation error remains within 1% for fine meshes and 2-3% for coarse ones. The results of an extensive parametric study also suggests that an optimum mesh-dependent domain radius exists at which the SIF computation error hits its minimum. This optimum radius is roughly equal to

the nominal size of the elements at the crack front region. It was also shown that employing quarter-point tetrahedral elements can improve the FE solution of the crack tip fields significantly. These results provide further evidence of the applicability, efficiency and accuracy of unstructured meshes to analyze cracked bodies.

Acknowledgement

The authors thank Rio Tinto for supporting this work, through the Rio Tinto Center for Advanced Mineral Recovery at Imperial College London. They also thank the European Commission for partially funding this work through the TRUST Collaborative Project, 309067.

Appendix A. Auxiliary fields

It has been shown for 3D cracks that asymptotically, as $r \rightarrow 0$, plane strain conditions prevail locally, so that the three-dimensional deformation fields approach the two-dimensional plane strain fields (Nakamura and Parks, 1988, 1989). Therefore, 2D plane strain fields can be employed to express the auxiliary fields near any point along the crack front. The so-called Williams series expansions describe the linear elastic stress fields for a 2D cracked plate subjected to an arbitrary load (Williams, 1957). In the region close to the crack tip, the first terms in these expansions are dominant. The auxiliary fields for 3D embedded cracks are therefore considered to be in the form of these singular fields in the plane strain condition ($\sigma_{33}^{\text{aux}} = \nu(\sigma_{11}^{\text{aux}} + \sigma_{22}^{\text{aux}})$). Eqs. (A.1) and (A.2) give these stress fields when in-plane and anti-plane loads are applied, respectively (Anderson, 2005).

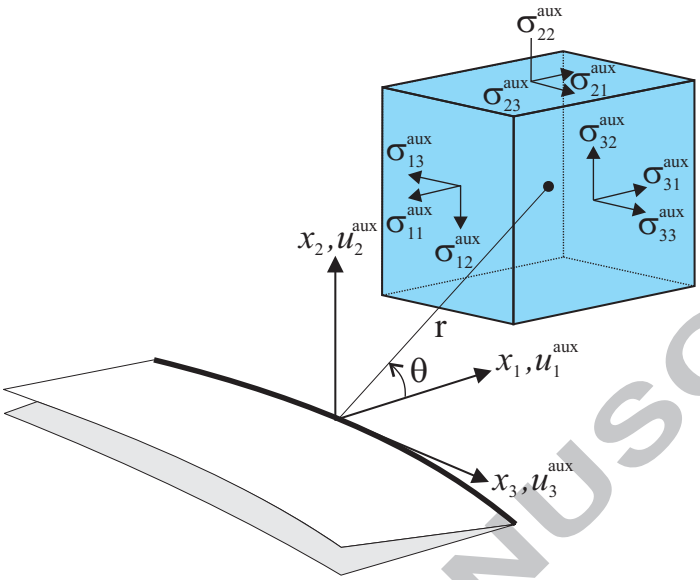

Figure A.1: Local Cartesian coordinate system at a point along crack front and crack tip auxiliary fields.

$$\begin{Bmatrix} \sigma_{11}^{\text{aux}} \\ \sigma_{22}^{\text{aux}} \\ \sigma_{12}^{\text{aux}} \\ \sigma_{33}^{\text{aux}} \end{Bmatrix} = \frac{K_{\text{I}}^{\text{aux}}}{\sqrt{2\pi r}} \begin{Bmatrix} \cos\frac{\theta}{2}\left(1 - \sin\frac{\theta}{2}\sin\frac{3\theta}{2}\right) \\ \cos\frac{\theta}{2}\left(1 + \sin\frac{\theta}{2}\sin\frac{3\theta}{2}\right) \\ \cos\frac{\theta}{2}\sin\frac{\theta}{2}\cos\frac{3\theta}{2} \\ 2\nu\cos\frac{\theta}{2} \end{Bmatrix} + \frac{K_{\text{II}}^{\text{aux}}}{\sqrt{2\pi r}} \begin{Bmatrix} \sin\frac{\theta}{2}\left(-2 - \cos\frac{\theta}{2}\cos\frac{3\theta}{2}\right) \\ \sin\frac{\theta}{2}\cos\frac{\theta}{2}\cos\frac{3\theta}{2} \\ \cos\frac{\theta}{2}\left(1 - \sin\frac{\theta}{2}\sin\frac{3\theta}{2}\right) \\ -2\nu\sin\frac{\theta}{2} \end{Bmatrix} \tag{A.1}$$

$$\begin{Bmatrix} \sigma_{13}^{\text{aux}} \\ \sigma_{23}^{\text{aux}} \end{Bmatrix} = \frac{K_{\text{III}}^{\text{aux}}}{\sqrt{2\pi r}} \begin{Bmatrix} -\sin\frac{\theta}{2} \\ \cos\frac{\theta}{2} \end{Bmatrix} \tag{A.2}$$

Here r and θ are the polar coordinates in a local Cartesian coordinate system $x_1x_2x_3$ which is perpendicular to the crack front, as shown in Fig. A.1. The displacement fields adjacent to the crack tip due to the in-plane and anti-plane loadings conditions, respectively, are given by

(Anderson, 2005)

$$\begin{Bmatrix} u_1^{\text{aux}} \\ u_2^{\text{aux}} \end{Bmatrix} = \frac{K_{\text{I}}^{\text{aux}}}{2\mu}\sqrt{\frac{r}{2\pi}}\begin{Bmatrix} \cos\frac{\theta}{2}\left(\kappa - 1 + 2\sin^2\frac{\theta}{2}\right) \\ \sin\frac{\theta}{2}\left((\kappa + 1 - 2\cos^2\frac{\theta}{2}\right) \end{Bmatrix} + \frac{K_{\text{II}}^{\text{aux}}}{2\mu}\sqrt{\frac{r}{2\pi}}\begin{Bmatrix} \sin\frac{\theta}{2}\left(1 + \kappa + 2\cos^2\frac{\theta}{2}\right) \\ \cos\frac{\theta}{2}\left(1 - \kappa + 2\sin^2\frac{\theta}{2}\right) \end{Bmatrix} \tag{A.3}$$

$$u_3^{\text{aux}} = \frac{2K_{\text{III}}^{\text{aux}}}{\mu}\sqrt{\frac{r}{2\pi}}\sin\frac{\theta}{2} \tag{A.4}$$

where κ is a function of Poisson's ratio, and under plane strain conditions, $\kappa = 3 - 4\nu$. Under plane strain conditions, the out-of-plane displacement u_3^{aux} vanishes when applying in-plane loads, and in-plane displacements (u_1^{aux} and u_2^{aux}) are zero when anti-plane loads are applied. The derivatives of the displacement fields with respect to x_1 are readily obtained from Eqs. (A.3) and (A.4) as

$$\begin{Bmatrix} \frac{\partial u_1^{\text{aux}}}{\partial x_1} \\ \frac{\partial u_2^{\text{aux}}}{\partial x_1} \end{Bmatrix} = \frac{K_{\text{I}}^{\text{aux}}}{4\mu\sqrt{2\pi r}}\begin{Bmatrix} \cos\frac{\theta}{2}\left(\kappa - 1 - \cos\theta + \cos 2\theta\right) \\ \sin\frac{\theta}{2}\left(-\kappa - 1 + \cos\theta + \cos 2\theta\right) \end{Bmatrix} + \frac{K_{\text{II}}^{\text{aux}}}{4\mu\sqrt{2\pi r}}\begin{Bmatrix} -\sin\frac{\theta}{2}\left(\kappa + 1 + \cos\theta + \cos 2\theta\right) \\ \cos\frac{\theta}{2}\left(-\kappa + 1 - \cos\theta + \cos 2\theta\right) \end{Bmatrix} \tag{A.5}$$

$$\frac{\partial u_3^{\text{aux}}}{\partial x_1} = -\frac{K_{\text{III}}^{\text{aux}}}{\mu\sqrt{2\pi r}}\sin\frac{\theta}{2} \tag{A.6}$$

Appendix B. The performance of quarter-point virtual elements in integrating singular functions

The line and area integrals in Eqs. (17) and (20) include singular terms of types $1/\sqrt{r}$, and $1/r$, respectively. This section explains how placing the mid-side nodes at the quarter-point position near the crack tip leads to a more accurate numerical integration of these singular functions.

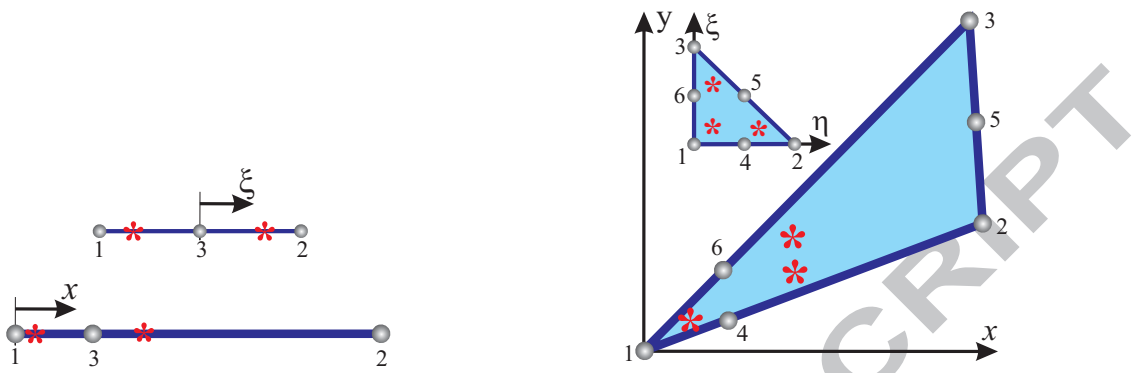

Figure B.1: Configuration of nodes and integration points in (a) quarter-point line element and (b) quarter-point triangular element.

Consider $x_1 = 0$, $x_2 = L$, and $x_3 = L/4$ being the positions of nodes 1, 2 and 3 of the isoparametric quarter-point line element shown in Fig. B.1a. Considering the element shape functions $N_1 = \xi(\xi - 1)/2$, $N_2 = \xi(\xi + 1)/2$, $N_3 = (1 - \xi)(1 + \xi)$, the mapping of the geometry from the local coordinate system x into the natural element coordinate system ξ, where $-1 \leq \xi \leq +1$, is given by $x(\xi) = \sum_{i=1}^{3} N_i x_i = (\xi + 1)^2 L/4$. This mapping has a Jacobian of $\partial x/\partial\xi = (\xi + 1)L/2$, which cancels out the square-root singular term in the integrand ($\int_0^L \mathrm{d}x/\sqrt{x} = \int_{-1}^{+1} \sqrt{L}\mathrm{d}\xi$). The standard quadrature rule is now able to compute the exact value of the integral.

Consider now that the corner nodes 1, 2 and 3 of the quarter-point triangular element shown in Fig. B.1b are located at $(0, 0)$, (x_2, y_2), and (x_3, y_3), respectively. The positions of the mid-side node 5 and the quarter-point nodes 4 and 6 are $((x_2 + x_3)/2, (y_2 + y_3)/2)$, $(x_2/4, y_2/4)$, and $(x_3/4, y_3/4)$, respectively. Considering the natural coordinates $0 \leq \xi \leq 1$, $0 \leq \eta \leq 1$ and $\gamma = 1 - \xi - \eta$, the element shape functions are $N_1 = \gamma(2\gamma - 1)$, $N_2 = \xi(2\xi - 1)$, $N_3 = \eta(2\eta - 1)$, $N_4 = 4\gamma\xi$, $N_5 = 4\xi\eta$, $N_6 = 4\gamma\eta$, and the mapping of the geometry from the local coordinate system xy into the natural coordinate system $\xi\eta$ is given by

$$
\begin{aligned}
x(\xi,\eta) &= \textstyle\sum_{i=1}^{6} N_i x_i = (\xi+\eta)(\xi x_2 + \eta x_3) \\
y(\xi,\eta) &= \textstyle\sum_{i=1}^{6} N_i x_i = (\xi+\eta)(\xi y_2 + \eta y_3) \\
r(\xi,\eta) &= (\xi+\eta)^2 \sqrt{\left[\frac{\xi x_2 + \eta x_3}{\xi+\eta}\right]^2 + \left[\frac{\xi y_2 + \eta y_3}{\xi+\eta}\right]^2}
\end{aligned}
\tag{B.1}
$$

where r denotes the radial distance from the node 1 (crack tip). This mapping gives the determinant of the Jacobian matrix $\mathbf{J} = \partial(x,y)/\partial(\xi,\eta)$ as $|\mathbf{J}| = 2(\xi+\eta)^2(x_2y_3 - x_3y_2)$ which cancels out the singular term in the integrand:

$$
\int_A \frac{\mathrm{d}A}{r} = \int_0^1 \int_0^1 \frac{2(x_2y_3 - x_3y_2)}{\sqrt{\left[\frac{\xi x_2 + \eta x_3}{\xi+\eta}\right]^2 + \left[\frac{\xi y_2 + \eta y_3}{\xi+\eta}\right]^2}} \mathrm{d}\xi \mathrm{d}\eta \tag{B.2}
$$

in which A is the area of the triangular element. This transformation significantly improves the accuracy of the numerical integration by a standard quadrature-rule procedure. In fact, the integration points are placed closer to the singular point in quarter-point elements, which helps them to efficiently capture the high gradients of singular integrands near the singular point.

Appendix C. Obtaining field values at a given point in tetrahedral/triangular elements

The evaluation of J- and interaction integrals using the proposed disk-shaped domain integral method requires the computation of the field values at a given point inside tetrahedra or triangles. In order to obtain the field values at the given point p first the tetrahedral or triangular element containing it must be identified through a search algorithm. Then, the natural coordinates of that given point inside the element must be determined. The fields can then be readily obtained through the shape functions.

Appendix C.1. Tetrahedral element

An unstructured mesh of a 3D cracked body mainly generates two types of tetrahedral elements surrounding the crack front: (i) tetrahedral elements which share a corner node with the

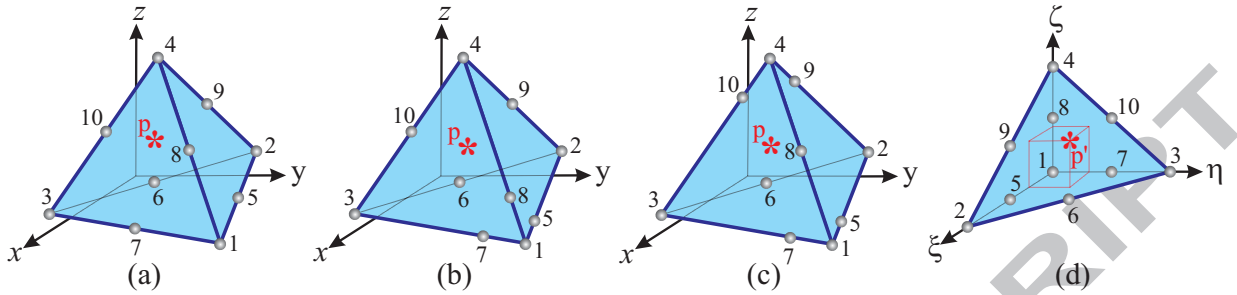

Figure C.1: Mapping of the point p inside (a) standard quadratic tetrahedral, (b) corner-based quarter-point tetrahedral (CQPT), and (c) edge-based quarter-point tetrahedral (EQPT) from global coordinate system xyz to point p' inside (d) parent tetrahedral element in natural system $\xi\eta\zeta$.

crack front; (ii) tetrahedra which share an edge with the crack front. Accordingly, shifting the mid-side nodes near the crack front to the quarter-point position generates two types of quarter-point elements: (i) corner-based quarter-point tetrahedra (CQPT); and (ii) edge-based quarter-point tetrahedra (EQPT). Consider a tetrahedral element of any type with straight edges as shown in Fig. C.1a,b,c. The corner node i of these elements has the coordinates (x_i, y_i, z_i), and the point p is located at $(x_\mathrm{p}, y_\mathrm{p}, z_\mathrm{p})$ in the global coordinate system xyz. The volume of the tetrahedral element V is computed by the determinant given in Eq. (C.1). The volumes of smaller internal tetrahedrals which are generated with one face of the main tetrahedral and the point p are also computed from the determinants in Eq. (C.2). The point p is inside the tetrahedral element if all the determinants, or volumes, in Eq. (C.2) are non-negative ($V_i \geq 0$).

$$V = \frac{1}{6}\begin{vmatrix} x_2 & y_2 & z_2 & 1 \\ x_3 & y_3 & z_3 & 1 \\ x_4 & y_4 & z_4 & 1 \\ x_1 & y_1 & z_1 & 1 \end{vmatrix} \tag{C.1}$$

$$V_1 = \frac{1}{6}\begin{vmatrix} x_2 & y_2 & z_2 & 1 \\ x_3 & y_3 & z_3 & 1 \\ x_4 & y_4 & z_4 & 1 \\ x_p & y_p & z_p & 1 \end{vmatrix}, \; V_2 = \frac{1}{6}\begin{vmatrix} x_p & y_p & z_p & 1 \\ x_3 & y_3 & z_3 & 1 \\ x_4 & y_4 & z_4 & 1 \\ x_1 & y_1 & z_1 & 1 \end{vmatrix}, \; V_3 = \frac{1}{6}\begin{vmatrix} x_2 & y_2 & z_2 & 1 \\ x_p & y_p & z_p & 1 \\ x_4 & y_4 & z_4 & 1 \\ x_1 & y_1 & z_1 & 1 \end{vmatrix}, \; V_4 = \frac{1}{6}\begin{vmatrix} x_2 & y_2 & z_2 & 1 \\ x_3 & y_3 & z_3 & 1 \\ x_p & y_p & z_p & 1 \\ x_1 & y_1 & z_1 & 1 \end{vmatrix} \tag{C.2}$$

The point p inside any type of tetrahedral element in Fig. C.1a,b,c is mapped to the point p' inside the parent tetrahedral element shown in Fig. C.1d. In the case of standard tetrahedral element in Fig. C.1a, the global coordinates are mapped linearly into the natural ones through Eq. (C.3). Solving these equations for the natural coordinates gives the coordinates of p' as volume fractions in Eq. (C.4):

$$\begin{aligned} x &= x_1 + (x_2 - x_1)\xi + (x_3 - x_1)\eta + (x_4 - x_1)\zeta \\ y &= y_1 + (y_2 - y_1)\xi + (y_3 - y_1)\eta + (y_4 - y_1)\zeta \\ z &= z_1 + (z_2 - z_1)\xi + (z_3 - z_1)\eta + (z_4 - z_1)\zeta \end{aligned} \tag{C.3}$$

$$\xi_{p'} = \frac{V_2}{V} \;\; , \;\; \eta_{p'} = \frac{V_3}{V} \;\; , \;\; \zeta_{p'} = \frac{V_4}{V} \tag{C.4}$$

In the case of quarter-point tetrahedrals, however, careful attention is required, as the mapping is not linear, and the volume fractions in Eq. (C.4) are no longer valid for the computation of the natural coordinates. In addition, these types of elements have specific orientations, which need to be taken into account. Assume the orientations shown in Fig. C.1b,c, which renders the midside nodes 5,7, and 8 for the CQPT moved to the quarter-point position from node 1, and the nodes and 5,7,9, and 10 for the EQPT moved to the quarter-point position from nodes 1 and 4. The mapping functions are developed as Eqs. (C.5) and (C.6) for the CQPT and EQPT, respectively. Solving these equations for non-negative natural coordinates, and simplifying the resulting algebraic equations give the natural coordinates of p' for CQPT and EQPT through Eqs.

(C.7) and (C.8), respectively.

$$\begin{aligned} x &= x_1 + (\xi+\eta+\zeta)[(x_2-x_1)\xi + (x_3-x_1)\eta + (x_4-x_1)\zeta] \\ y &= y_1 + (\xi+\eta+\zeta)[(y_2-y_1)\xi + (y_3-y_1)\eta + (y_4-y_1)\zeta] \\ z &= z_1 + (\xi+\eta+\zeta)[(z_2-z_1)\xi + (z_3-z_1)\eta + (z_4-z_1)\zeta] \end{aligned} \tag{C.5}$$

$$\begin{aligned} x &= x_1 + (\xi+\eta)[(x_2-x_1)\xi + (x_3-x_1)\eta] + (x_4-x_1)(1+\xi+\eta)\zeta \\ y &= y_1 + (\xi+\eta)[(y_2-y_1)\xi + (y_3-y_1)\eta] + (y_4-y_1)(1+\xi+\eta)\zeta \\ z &= z_1 + (\xi+\eta)[(z_2-z_1)\xi + (z_3-z_1)\eta] + (z_4-z_1)(1+\xi+\eta)\zeta \end{aligned} \tag{C.6}$$

$$\xi_{p'} = \frac{V_2}{\sqrt{V(V-V_1)}} \quad , \quad \eta_{p'} = \frac{V_3}{\sqrt{V(V-V_1)}} \quad , \quad \zeta_{p'} = \frac{V_4}{\sqrt{V(V-V_1)}} \tag{C.7}$$

$$\xi_{p'} = \frac{V_2}{\sqrt{V(V_2+V_3)}} \quad , \quad \eta_{p'} = \frac{V_3}{\sqrt{V(V_2+V_3)}} \quad , \quad \zeta_{p'} = \frac{V_4}{V+\sqrt{V(V_2+V_3)}} \tag{C.8}$$

Once the local coordinates are known, the displacements of the point p are obtained by interpolating the values of nodal displacements. The displacement gradients and strains are also determined by substituting the natural coordinates in the so-called B matrix. The stress tensor is then computed from the strains using $\sigma = \mathbf{D}\varepsilon$, where $\mathbf{D}$ is the elasticity matrix containing the material properties.

Appendix C.2. Triangular element

Due to moving of the mid-side nodes to the quarter-point position at the crack front region, two types of quarter-points triangles are also developed at the crack surfaces: corner-based quarter-point triangles (CQPTr) which share one node with the crack front, and edge-based quarter-point triangles (EQPTr) which share one edge with the crack front. Consider a planar triangular element of any type with straight edges on the crack surfaces as shown in Fig. C.2a,b,c. The corner node i of these elements has the coordinates (x_i, y_i, z_i), and the point p lies on the crack surface, locating at (x_p, y_p, z_p) in the global coordinate system xyz. The normal vector to these elements

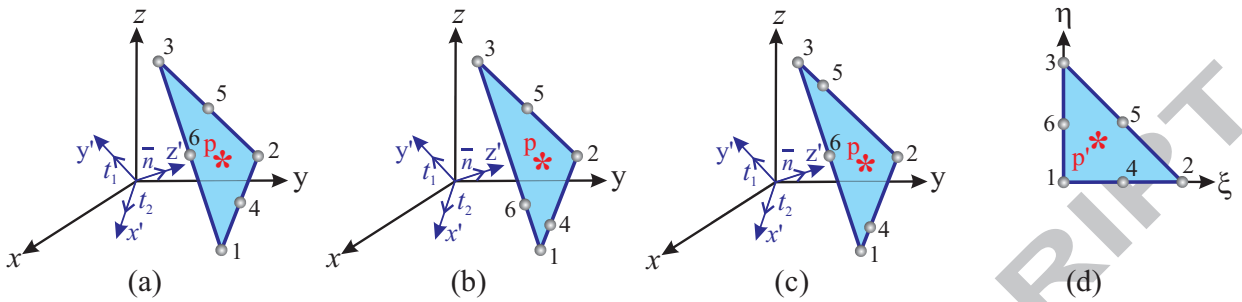

Figure C.2: Mapping of point p inside (a) standard quadratic triangle, (b) corner-based quarter-point trianlge (CQPTr), and (c) edge-based quarter-point triangle (EQPTr) from global coordinate system xyz to point p' inside (d) parent triangle element in natural coordinate system $\xi\eta$ ($\bar{n} = n/|n|$).

($n = (n_x, n_y, n_z)$) is computed from Eq. (C.9), and the area of the triangular element A is determined by the determinant given in Eq. (C.10). The area of smaller internal triangles which are generated with one edge of the main triangle and the point p are also computed from the determinants in Eq. (C.11). The point p is inside the triangle element if all the determinants in Eq. (C.11) are non-negative ($A_i \geq 0$).

$$n_x = \begin{vmatrix} 1 & 0 & 0 & 0 \\ x_2 & y_2 & z_2 & 1 \\ x_3 & y_3 & z_3 & 1 \\ x_1 & y_1 & z_1 & 1 \end{vmatrix}, \quad n_y = \begin{vmatrix} 0 & 1 & 0 & 0 \\ x_2 & y_2 & z_2 & 1 \\ x_3 & y_3 & z_3 & 1 \\ x_1 & y_1 & z_1 & 1 \end{vmatrix}, \quad n_z = \begin{vmatrix} 0 & 0 & 1 & 0 \\ x_2 & y_2 & z_2 & 1 \\ x_3 & y_3 & z_3 & 1 \\ x_1 & y_1 & z_1 & 1 \end{vmatrix} \tag{C.9}$$

$$A = \frac{1}{2|n|} \begin{vmatrix} n_x & n_y & n_z & 0 \\ x_2 & y_2 & z_2 & 1 \\ x_3 & y_3 & z_3 & 1 \\ x_1 & y_1 & z_1 & 1 \end{vmatrix} \tag{C.10}$$

$$A_1 = \frac{1}{2|n|}\begin{vmatrix} n_x & n_y & n_z & 0 \\ x_2 & y_2 & z_2 & 1 \\ x_3 & y_3 & z_3 & 1 \\ x_p & y_p & z_p & 1 \end{vmatrix},\ A_2 = \frac{1}{2|n|}\begin{vmatrix} n_x & n_y & n_z & 0 \\ x_p & y_p & z_p & 1 \\ x_3 & y_3 & z_3 & 1 \\ x_1 & y_1 & z_1 & 1 \end{vmatrix},\ A_3 = \frac{1}{2|n|}\begin{vmatrix} n_x & n_y & n_z & 0 \\ x_2 & y_2 & z_2 & 1 \\ x_p & y_p & z_p & 1 \\ x_1 & y_1 & z_1 & 1 \end{vmatrix} \tag{C.11}$$

Using the shape functions of a quadratic triangular element in Eq. (C.12), the point p inside any type of triangular elements in Fig. C.2a,b,c is mapped to the point p' inside the parent triangle element shown in Fig. C.2d ($\lambda = 1 - \xi - \eta$). Consider two arbitrary unit vectors t_1 and t_2 which lie on the plane passing through element face in a way that three vector t_1, t_2, and n build a right-handed Cartesian coordinate system $x'y'z'$ ($n = t_1 \times t_2$). Also consider the vectors $r_p = (x_p, y_p, z_p)$, and $r_i = (x_i, y_i, z_i), i = 1, 2, 3$. The mapping function of a standard triangular element in Fig. C.2a from $x'y'z'$ space to $\xi\eta$ space is therefore obtained as Eq. (C.13). Solving these equations for the natural coordinates and simplifying the resulting equations using $t_1 \times t_2 = n/|n|$ give the coordinates of p' as the area fractions in Eq. (C.14):

$$N_1 = \lambda(2\lambda - 1)\ ,\ N_2 = \xi(2\xi - 1)\ ,\ N_3 = \eta(2\eta - 1)\ ,\ N_4 = 4\lambda\xi\ ,\ N_5 = 4\xi\eta\ ,\ N_6 = 4\lambda\eta \tag{C.12}$$

$$\begin{aligned} x' &= t_1.r_p = t_1.r_1 + t_1.(r_2 - r_1)\xi + t_1.(r_3 - r_1)\eta \\ y' &= t_2.r_p = t_2.r_1 + t_2.(r_2 - r_1)\xi + t_2.(r_3 - r_1)\eta \\ z' &= n.r_p = n.r_1 \end{aligned} \tag{C.13}$$

$$\xi_p = \frac{A_2}{A}\ \ ,\ \ \eta_p = \frac{A_3}{A} \tag{C.14}$$

In the case of quarter-point triangles, special attention is required as the mapping is no longer

linear and these elements have specific orientations. Assume the orientations shown in Fig. C.2b,c, which renders the midside nodes 4 and 6 in the CQPTr are moved to the quarter-point position from node 1, and the nodes 4 and 5 for the EQPTr are moved to the quarter-point positions from nodes 1 and 3, respectively. Using the shape functions in Eq. (C.12), the mapping functions are developed as Eqs. (C.15) and (C.16) for the CQPTr and EQPTr elements, respectively. Solving these equations for non-negative natural coordinates and simplifying the resulting algebraic equations give the natural coordinates of p' for CQPTr and EQPTr through Eqs. (C.17) and (C.18), respectively.

$$\begin{aligned} x' &= t_1.r_p = t_1.r_1 + \left[t_1.(r_2 - r_1)\xi + t_1.(r_3 - r_1)\eta\right](\xi + \eta) \\ y' &= t_2.r_p = t_2.r_1 + \left[t_2.(r_2 - r_1)\xi + t_2.(r_3 - r_1)\eta\right](\xi + \eta) \\ z' &= n.r_p = n.r_1 \end{aligned} \tag{C.15}$$

$$\begin{aligned} x' &= t_1.r_p = t_1.r_1 + t_1.(r_2 - r_1)\xi^2 + t_1.(r_3 - r_1)(\xi + 1)\eta \\ y' &= t_2.r_p = t_2.r_1 + t_2.(r_2 - r_1)\xi^2 + t_2.(r_3 - r_1)(\xi + 1)\eta \\ z' &= n.r_p = n.r_1 \end{aligned} \tag{C.16}$$

$$\xi_{p'} = \frac{A_2}{\sqrt{A(A_2 + A_3)}} \quad , \quad \eta_{p'} = \frac{A_3}{\sqrt{A(A_2 + A_3)}} \tag{C.17}$$

$$\xi_{p'} = \sqrt{\frac{A_2}{A}} \quad , \quad \eta_{p'} = \frac{A_3}{A + \sqrt{AA_2}} \tag{C.18}$$

Once the local coordinates are known, the displacements of the point p are obtained by interpolating the values of nodal displacements using triangle shape functions in Eq. (C.12) and $u = \sum_{i=1}^{6} N_i u_i, v = \sum_{i=1}^{6} N_i v_i, w = \sum_{i=1}^{6} N_i w_i$. The surface tractions are also computed in the same way using the values of tractions at the nodes. The nodal tractions may be known through predefined boundary conditions, or the FE results of a contact treatment on the crack surfaces.

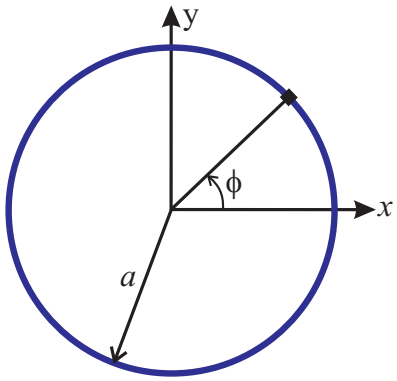

(c)

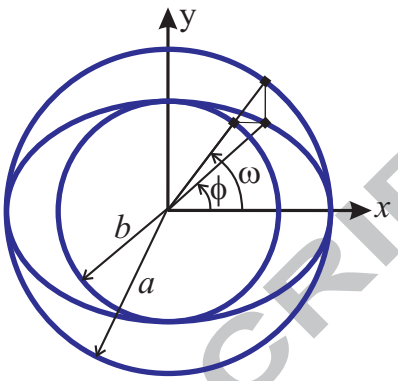

(d)

Figure D.1: Configurations of (a) penny-shaped and (b) elliptical cracks.

Appendix D. Stress intensity factors for an embedded penny-shaped/elliptical crack in an infinite body under uniaxial tension

Analytical solutions for the SIFs of penny-shaped and elliptical cracks embedded in infinite solids subjected to uniform tension or shear have been derived in Kassir and Sih (1975). Consider an inclined penny-shaped/elliptical crack embedded in a solid under uniaxial tension σ, as shown in Fig. 6b. The crack plane is perpendicular to the X_1X_2 plane, and makes an angle β with the applied load direction which is oriented along the X_2 axis. The normal and shear stress components on the crack face are $\sigma_{zz} = \sigma \sin^2\beta$ and $\sigma_{zx} = \sigma \sin\beta\cos\beta$. The SIFs of the penny-shaped crack are therefore given by

$$
\begin{aligned}
K_{\mathrm{I}} &= 2\sigma\sqrt{a/\pi}\sin^2\beta \\
K_{\mathrm{II}} &= \frac{2\sigma\sqrt{a/\pi}}{2-\nu}\sin 2\beta\cos\phi \\
K_{\mathrm{III}} &= \frac{2(1-\nu)\sigma\sqrt{a/\pi}}{2-\nu}\sin 2\beta\sin\phi
\end{aligned}
\tag{D.1}
$$

where a and ν are the crack radius and Poisson's ratio, respectively, and ϕ is the polar angle, as shown in Fig. D.1a. It should be noted that incorrect solutions for the SIFs of penny-shaped cracks were reported by Cherepanov (1979). These solutions, which do not contain Poisson's ratio, were

incorrectly employed to validate the numerical results by Nikishkov and Atluri (1987b). The SIFs of the elliptical crack are given by

$$\begin{aligned} K_{\mathrm{I}}(\omega) &= \frac{\sigma\sqrt{\pi a}}{E(k)}\sin^2\beta\,\Pi(\omega) \\ K_{\mathrm{II}}(\omega) &= \frac{\Psi k'\sigma\sqrt{\pi a}}{2\Pi(\omega)}\sin 2\beta\cos\omega \\ K_{\mathrm{III}}(\omega) &= \frac{\Psi(1-\nu)\sigma\sqrt{\pi a}}{2\Pi(\omega)}\sin 2\beta\sin\omega \end{aligned} \tag{D.2}$$

where

$$\begin{aligned} \Psi &= \frac{k^2 k'}{(k^2-\nu)E(k)+\nu k'^2 K(k)} \\ \Pi(\omega) &= \left(k'^2\sin^2\omega + k'^4\cos^2\omega\right)^{1/4} \end{aligned} \tag{D.3}$$

In these formulas, $k' = b/a$, $k^2 = 1 - k'^2$, a and b are the lengths of semi-major and semi-minor axes of the ellipse ($a > b$), and $K(k)$ and $E(k)$ are the complete first and second elliptic integrals, given by

$$\begin{aligned} K(k) &= \int_0^{\pi/2} \frac{1}{\sqrt{1-k^2\sin^2 t}}\,\mathrm{d}t \\ E(k) &= \int_0^{\pi/2} \sqrt{1-k^2\sin^2 t}\,\mathrm{d}t \end{aligned} \tag{D.4}$$

Angle ω parameterizes the points of the ellipse by the equations $x = a\cos\omega, y = b\sin\omega$, and is related to the polar angle ϕ by $k'\tan\omega = \tan\phi$ (see Fig. D.1b). Rewriting Eq. (D.4) in terms of the polar angle ϕ gives (Kachanov et al., 2003):

$$
\begin{aligned}
K_{\mathrm{I}}(\phi) &= \frac{k'\sigma\sqrt{\pi a}}{E(k)}\,\frac{\Pi_1(\phi)}{\Pi_2(\phi)}\sin^2\beta \\
K_{\mathrm{II}}(\phi) &= \frac{\Psi k'^2\sigma\sqrt{\pi a}}{2\Pi_1(\phi)\Pi_2(\phi)}\sin 2\beta\cos\phi \\
K_{\mathrm{III}}(\phi) &= \frac{\Psi(1-\nu)\sigma\sqrt{\pi a}}{2\Pi_1(\phi)\Pi_2(\phi)}\sin 2\beta\sin\phi
\end{aligned}
\tag{D.5}
$$

where

$$
\begin{aligned}
\Pi_1(\phi) &= \left(\sin^2\phi + k'^4\cos^2\phi\right)^{1/4} \\
\Pi_2(\phi) &= \left(k'^2\sin^2\phi + k'^4\cos^2\phi\right)^{1/4}
\end{aligned}
\tag{D.6}
$$

References

References

Abaqus, 2012. ABAQUS User's Manual, Version 6.12 Documentation. Dassault Systemes Simulia Corp. Providence, RI, USA.

Anderson, T., 2005. Fracture Mechanics, Fundamentals and Applications. CRC, Boca Raton.

Ayatollahi, M., Aliha, M., Hassani, M., 2006. Mixed mode brittle fracture in PMMA - An experimental study using SCB specimens. Materials Science and Engineering A 417, 348–356.

Ayatollahi, M., Nejati, M., 2011a. An over-deterministic method for calculation of coefficients of crack tip asymptotic field from finite element analysis. Fatigue & Fracture of Engineering Materials & Structures 34 (3), 159–176.

Ayatollahi, M., Nejati, M., 2011b. Determination of NSIFs and coefficients of higher order terms for sharp notches using finite element method. International Journal of Mechanical Sciences 53 (3), 164–177.

Banks-Sills, L., 2010. Update: Application of the Finite Element Method to Linear Elastic Fracture Mechanics. Applied Mechanics Reviews 63 (2), 020803.

Banks-Sills, L., Sherman, D., 1992. On the computation of stress intensity factors for three-dimensional geometries by means of the stiffness derivative and J-integral methods. International Journal of Fracture 53 (1), 1–20.

Barsoum, R., 1976. On the use of isoparametric finite elements in linear fracture mechanics. International Journal for Numerical Methods in Engineering 10, 25–37.

Bažant, Z., Estenssoro, L., 1979. Surface singularity and crack propagation. International Journal of Solids and Structures 15, 405–426.

Benthem, J., 1977. State of stress at the vertex of a quarter-infinite crack in a half-space. International Journal of Solids and Structures 13 (5), 479–492.

Benthem, J., 1980. The quarter-infinite crack in a half space; Alternative and additional solutions. International Journal of Solids and Structures 16, 119–130.

Berto, F., Lazzarin, P., 2010. On higher order terms in the crack tip stress field. International Journal of Fracture 161, 221–226.

Bremberg, D., Dhondt, G., 2008. Automatic crack-insertion for arbitrary crack growth. Engineering Fracture Mechanics 75, 404–416.

Bremberg, D., Dhondt, G., 2009. Automatic 3-D crack propagation calculations: a pure hexahedral element approach versus a combined element approach. International Journal of Fracture 157 (1-2), 109–118.

Bremberg, D., Faleskog, J., 2015. A numerical procedure for interaction integrals developed for curved cracks of general shape in 3-D. International Journal of Solids and Structures 62, 144–157.

Budiansky, B., Rice, J., 1973. Conservation laws and energy-release rates. Journal of Applied Mechanics 40, 201–203.

Bui, H., 1983. Associated path independent J-integrals for separating mixed modes. Journal of the Mechanics and Physics of Solids 31 (6), 439–448.

Chan, S., Tuba, I., Wilson, W., 1970. On the finite element method in linear fracture mechanics. Engineering Fracture Mechanics M (1).

Chen, F., Shield, R., 1977. Conservation laws in elasticity of the J-integral type. Journal of Applied Mathematics and Physics 28 (1), 1–22.

Cherepanov, G., 1967. Crack propagation in continuous media. Journal of Applied Mathematics and Mechanics 31, 503–512.

Cherepanov, G., 1979. Mechanics of brittle fracture. McGraw-Hill, New York.

Daimon, R., Okada, H., 2014. Mixed-mode stress intensity factor evaluation by interaction integral method for quadratic tetrahedral finite element with correction terms. Engineering Fracture Mechanics 115, 22–42.

DeLorenzi, H., 1982. On the energy release rate and the J-integral for 3-D crack configurations. International Journal of Fracture 19, 183–193.

Eshelby, J., 1970. Inelastic Behavior of Solids. McGraw-Hill, New York.

Gosz, M., Dolbow, J., Moran, B., 1998. Domain integral formulation for stress intensity factor computation along curved three-dimensional interface cracks. International Journal of Solids and Structures 35 (15), 1763–1783.

Gosz, M., Moran, B., 2002. An interaction energy integral method for computation of mixed-mode stress intensity factors along non-planar crack fronts in three dimensions. Engineering Fracture Mechanics 69 (3), 299–319.

Harding, S., Kotousov, A., Lazzarin, P., Berto, F., 2010. Transverse singular effects in V-shaped notches stressed in mode II. International Journal of Fracture 164 (1), 1–14.

He, Z., Kotousov, A., Berto, F., 2015. Effect of vertex singularities on stress intensities near plate free surfaces. Fatigue & Fracture of Engineering Materials & Structures, DOI: 10.1111/ffe.12294.

Henshell, R., Shaw, K., 1975. Crack tip finite elements are unnecessary. International Journal for Numerical Methods in Engineering 9, 495–507.

Huber, O., Nickel, J., Kuhn, G., 1993. On the decomposition of the J-integral for 3D crack problems. International Journal of Fracture 64 (4), 339–348.

Ingraffea, A., Manu, C., 1980. Stress intensity factor computation in three dimensions with quarter-point elements. International Journal for Numerical Methods in Engineering 15, 1427–1445.

Irwin, G., 1956. Onset of fast crack propagation in high steel and aluminium alloys. Sagamore Research Conference Proceedings 2, 289–305.

Kachanov, M., Shafiro, B., Tsukrov, I., 2003. Handbook of elasticity solutions. Kluwer Academic Publishers, Dordrecht.

Kassir, M., Sih, G., 1975. Mechanics of fracture 2: three-dimensional crack problems. Noordhoff International Publishing, Leyden.

Kfouri, A., 1986. Some evaluations of the elastic T-term using Eshelby's method. International Journal of Fracture 30, 301–315.

Kim, Y., Kim, H., Im, S., 2001. Mode decomposition of three-dimensional mixed-mode cracks via two-state integrals. International Journal of Solids and Structures 38, 6405–6426.

Kotousov, A., Lazzarin, P., Berto, F., Harding, S., 2010. Effect of the thickness on elastic deformation and quasi-brittle fracture of plate components. Engineering Fracture Mechanics 77 (11), 1665–1681.

Kotousov, a., Lazzarin, P., Berto, F., Pook, L., 2013. Three-dimensional stress states at crack tip induced by shear and anti-plane loading. Engineering Fracture Mechanics 108, 65–74.

Kuna, M., 2013. Finite Elements in Fracture Mechanics: Theory - Numerics - Applications). Springer, Dordrecht.

Li, F., Shih, C., Needleman, A., 1985. A comparison of methods for calculating energy release rates. Engineering Fracture Mechanics 21 (2), 405–421.

Matthai, S., Geiger, S., Roberts, S., 2001. The complex systems platform CSP3D3.0: Users Guide. Technical report, ETH Zurich Research Reports.

Moran, B., Shih, C., 1987a. A general treatment of crack tip contour integrals. International Journal of Fracture 35 (4), 295–310.

Moran, B., Shih, C., 1987b. Crack tip and associated domain integrals from momentum and energy balance. Engineering Fracture Mechanics 27 (6), 615–642.

Nahta, R., Moran, B., 1993. Domain integrals for axisymmetric interface crack problems. International Journal of Solids and Structures 30 (15), 2027–2040.

Nakamura, T., Parks, D., 1988. Three-dimensional stress field near the crack front of a thin elastic plate. Journal of Applied Mechanics 55, 805–813.

Nakamura, T., Parks, D., 1989. Antisymmetrical 3-D stress field near the crack front of a thin elastic plate. International Journal of Solids and Structures 25 (12), 1411–1426.

Nikishkov, G., Atluri, S., 1987a. An equivalent domain integral method for computing crack-tip integral parameters in non-elastic, thermo-mechanical fracture. Engineering Fracture Mechanics 26 (6), 851–867.

Nikishkov, G., Atluri, S., 1987b. Calculation of fracture mechanics parameters for an arbitrary three-dimensional crack, by the 'equivalent domain integral' method. International Journal for Numerical Methods in Engineering 24 (9), 1801–1821.

Okada, H., Kawai, H., Araki, K., 2008. A virtual crack closure-integral method (VCCM) to compute the energy release rates and stress intensity factors based on quadratic tetrahedral finite elements. Engineering Fracture Mechanics 75 (15), 4466–4485.

Paluszny, A., Matthäi, S. K., 2009. Numerical modeling of discrete multi-crack growth applied to pattern formation in geological brittle media. International Journal of Solids and Structures 46, 3383–3397.

Paluszny, A., Tang, X. H., Zimmerman, R. W., 2013. Fracture and impulse based finite-discrete element modeling of fragmentation. Computational Mechanics 52 (5), 1071–1084.

Paluszny, A., Zimmerman, R. W., 2011. Numerical simulation of multiple 3D fracture propagation using arbitrary meshes. Computer Methods in Applied Mechanics and Engineering 200, 953–966.

Parks, D., 1974. A stiffness derivative finite element technique for determination of crack tip stress intensity factors. International Journal of Fracture 10 (4), 487–502.

Pook, L., Berto, F., Campagnolo, A., Lazzarin, P., 2014. Coupled fracture mode of a cracked disc under anti-plane loading. Engineering Fracture Mechanics 128, 22–36.

Rajaram, H., Socrate, S., Parks, D., 2000. Application of domain integral methods using tetrahedral elements to the determination of stress intensity factors. Engineering Fracture Mechanics 66 (5), 455–482.

Raju, I., Shivakumar, K., 1990. An equivalent domain integral method in the two-dimensional analysis of mixed mode

crack problems. Engineering Fracture Mechanics 37 (4), 707–725.

Rice, J., 1968. A path independent integral and the approximate analysis of strain concentration by notches and cracks. Journal of Applied Mechanics 35, 379–386.

Rigby, R., Aliabadi, M., 1998. Decomposition of the mixed-mode J-integral-revisited. International Journal of Solids and Structures 35 (17), 2073–2099.

Rybicki, E., Kanninen, M., 1977. A finite element calculation of stress intensity factors by a modified crack closure integral. Engineering Fracture Mechanics 9, 931–938.

Schöllmann, M., Fulland, M., Richard, H., 2003. Development of a new software for adaptive crack growth simulations in 3D structures. Engineering Fracture Mechanics 70, 249–268.

Shih, C., Lorenzi, H., German, M., 1976. Crack extension modeling with singular quadratic isoparametric elements. International Journal of Fracture 12 (3), 647–651.

Shih, C., Moran, B., Nakamura, T., 1986. Energy release rate along a three-dimensional crack front in a thermally stressed body. International Journal of Fracture 30, 79–102.

Shivakumar, K., Raju, I., 1992. An equivalent domain integral method for three-dimensional mixed-mode fracture problems. Engineering Fracture Mechanics 42 (6), 935–959.

Smith, D., Ayatollahi, M., Pavier, M., 2001. The role of T-stress in brittle fracture for linear elastic materials under mixed-mode loading. Fatigue & Fracture of Engineering Materials & Structures 24, 137–150.

Stüben, K., 2001. A review of algebraic multigrid. Journal of Computational and Applied Mathematics 128, 281–309.

Toshio, N., Parks, D., 1992. Determination of elastic T-stress along three-dimensional crack fronts using an interaction integral. International Journal of Solids and Structures 29 (13), 1597–1611.

Červenka, J., Saouma, V., 1997. Numerical evaluation of 3-D SIF for arbitrary finite element meshes. Engineering Fracture Mechanics 57 (5), 541–563.

Walters, M., Paulino, G., Dodds, R., 2005. Interaction integral procedures for 3-D curved cracks including surface tractions. Engineering Fracture Mechanics 72 (11), 1635–1663.

Williams, M., 1957. On the stress distribution at the base of a stationary crack. Journal of Applied Mechanics 24, 109–114.

Yau, J., Wang, S., Corten, H., 1980. A mixed-mode crack analysis of isotropic solids using conservation laws of elasticity. Journal of Applied Mechanics 47, 335–341.